Single molecule tracking reveals nanodomains in biomolecular condensates

Author(s): *Guoming Gao[1,2], Emily R. Sumrall[1,2], Nils G. Walter[2,3*]*
Author affiliations:
[1]Biophysics Graduate Program, University of Michigan, Ann Arbor, MI 48109, USA
[2]Center for RNA Biomedicine, University of Michigan, Ann Arbor, MI 48109, USA
[3]Department of Chemistry, University of Michigan, Ann Arbor, MI 48109, USA
*Correspondence: nwalter@umich.edu

Abstract

Protein-rich biomolecular condensates formed by phase separation[1] play a crucial role in cellular RNA regulation by the selective recruitment and processing of RNA molecules[2]. The functional impact of condensates on RNA biology relies on the residence time of individual RNA molecules within a condensate[3], which is governed by intra-condensate diffusion[4] – the slower or more confined the diffusion, the longer the residence time. However, the spatiotemporal organization of RNA and protein diffusion within a single condensate remains largely unknown due to the challenge of accurately profiling intra-condensate diffusion behaviors down to the single-molecule level. Here we introduced a general condensate-tethering approach that allows single molecule tracking (SMT) of fluorescently labeled proteins and RNAs within non-wetted spherical 3D condensates without the interference of condensate motions. We found that a significant fraction of RNA and protein molecules are locally confined, rather than freely diffusive, within a model condensate formed by full-length, tag-free, RNA-binding protein Fused-in-Sarcoma (FUS), known for its critical roles in RNA biology under both physiological and pathological conditions[5]. Dynamic Point Accumulation for Imaging in Nanoscale Topography (PAINT)[6] reconstruction further revealed that RNA and proteins are confined to distinct slow-moving nanometer-scale regions, termed nanodomains, within a single condensate. Remarkably, nanodomains affect the diffusion but not the density of the confined biomolecules, supporting local percolation[1,7] rather than a secondary phase separation within the condensate as their origin. Beyond their regulatory roles on RNA residence time, nanodomains engender both elevated local connectivity and altered chemical environment, a prerequisite for pathological liquid-to-solid transition of FUS during aging. In summary, our study uncovers a patterned spatial organization of both protein and RNA molecules within a single condensate, revealing distinct diffusion dynamics that affect molecular retention time and interactions underlying cellular function and pathology.

Main

Both protein and RNA molecules can phase separate into biomolecular condensates that regulate cellular activities by organizing biochemical reactions[1,7-9]. Co-assembled ribonucleoprotein (RNP) granules play critical roles in RNA metabolism[2] such as transcription[10-12], splicing[12-14], translation[15,16], and decay[17,18] under both physiological and pathological conditions[9]. Proteins often serve as scaffold molecules that drive the phase separation, and RNAs usually partition into a condensate as guest molecules[8,19,20]. Cellular functions of RNP granules rely on the selective recruitment of RNA guest molecules and their corresponding processing machineries into condensates[1,2,8,19,20], as well as the resulting modulation of biochemical reaction rates[21,22]. Since all biological processes are time-dependent, information on how long an RNA molecule resides in a condensate and how the internal architecture of the condensate regulates intra-condensate diffusion are crucial, yet underexplored. Single-molecule tracking (SMT) by fluorescence microscopy has provided evidence of distinct interaction kinetics of RNAs with RNP granules in cells based on RNA functionality[3,23-25], but intracellular SMT generally lacks the spatiotemporal resolution needed to reveal intra-condensate diffusion. Complementary pioneering work using SMT *in vitro* has demonstrated different diffusive states and local chemical environments within condensates, with such measurements typically limited to proteins or organic dyes[26-33].

To gain deeper insight into the spatiotemporal organization of both protein scaffold and RNA guest molecules within RNP granules, we sought to identify and overcome the obstacles to accurate SMT within 3-dimensional (3D) condensates. Previous intra-condensate SMT experiments have been performed in condensates with protein[32] or RNA[34] components tethered to a membrane, forming flattened, wetted domains that have material properties distinct from those of spherical 3D condensates assembled via phase separation in bulk solution[35,36]. Even in the absence of membrane-tethering, condensates can still form wetted domains on glass surfaces due to non-specific protein absorption, which has not been systematically excluded in most studies[26-28,30,31]. Spherical 3D condensates can be preserved by proper surface passivation[33], but condensates on passivated glass surfaces can exhibit rotational or translational motions that interfere with the SMT of slowly diffusing molecules. Therefore, a system that both preserves 3D condensate shape and eliminates interference from whole-condensate motions is critical for accurate intra-condensate SMT.

Here we achieved accurate, simultaneous intra-condensate SMT of protein and RNA molecules by optimizing a general multi-tether approach that restricts condensate motion without inducing surface wetting. We chose Fused-in-Sarcoma (FUS) protein as our model RNP granule scaffold to assemble biomolecular condensates *in vitro*, since it regulates transcription, splicing, DNA-damage repair, and stress response by forming a variety of physiological and pathological condensates[5,37-40]. Notably, disease-related mutations of FUS have been linked to amyotrophic lateral sclerosis (ALS) and other neurodegenerative diseases, where mutants accelerate the liquid-to-solid phase transition of FUS condensates in a process termed aging, causing the pathological fibrilization of FUS within neurons[39,41-45]. We purified full-length tag-free FUS[46,47] to obtain condensates devoid of perturbations from protein truncations or purification tag and fluorescent protein appendages[48]. In contrast to the highly liquid-like material properties of these condensates, significant fractions of the constituting FUS scaffold molecules and model firefly luciferase (FL) messenger RNA (mRNA) guest molecules were found to be confined, rather than freely diffusive. Point Accumulation for Imaging in Nanoscale Topography (PAINT) reconstructions based on SMT trajectories directly visualized the underlying architecture that confines diffusion, defined by dynamic nanometer-scale regions within a single condensate. These nanodomains restrict the diffusion of molecules based on their size, shape, and charge,

leading to distinct protein and RNA diffusion behaviors within a condensate. The sub-condensate architecture observed here may form the basis for a spatial regulation of biochemical reactions that affect specific RNA and protein molecules in an RNP granule, including the fibrilization of FUS and aggregation of RNA.

Tethering enables SMT in liquid-like, full-length, tag-free FUS condensates

The N-terminal prion-like domain (PrLD, 1-239 aa) of FUS has been widely used as a model system to study phase separation[49-52]. We reasoned that the full-length protein contains C-terminal regions with structural and electrostatic features that may also affect condensate properties (Fig. 1a,b). To investigate condensates that most closely approximate a physiological scaffold protein behavior, we purified FUS in its full-length tag-free form, adapting a recently described protocol featuring multiple ion-exchange chromatography steps and an optimized refolding protocol with β-cyclodextran[46,47] (Fig. S1). In addition, the FL guest mRNA ~1,500 nucleotide (nt) in length was generated with the features necessary for intracellular translation, including a 5'-cap, a 5' untranslated region (UTR), and a poly-A tail (Fig. 1a, Fig. S1). For fluorescence-based SMT, we used click-chemistry to covalently attach minimally disruptive[53] organic dye molecules between the coding sequence and unmodified poly-A tail (Fig. 1a, Fig. S1). To characterize the phase separation of full-length tag-free FUS, we triggered condensation by diluting a stock solution of FUS to a physiological concentration of 10 μM FUS found in Hela cell nucleus[39]. Condensates were generally imaged within 30 minutes of assembly to avoid aging. We first determined the phase diagram (Fig. S2), which shows a binodal curve similar to previous reports for truncated or tagged FUS[39,54]. Next, we measured the condensate fusion kinetics using microrheology in a dual-trap optical tweezers setup (Fig. 1c). When the probing trap (purple, Fig. 1c) approaches the measurement trap (orange, Fig. 1c) at constant speed, the coalescence of the two condensates generates an increasing force on the measurement trap due to surface tension, accompanied by a decrease in total area of the condensates (Fig. 1c). The force curve upon transitioning from touching to fully fused droplets was used to extract the characteristic fusion time τ [39,54] (Fig. 1d). The distribution of τ values (Fig. 1e) exhibits significantly faster fusion ($\tau_{mean} = 51 \pm 4$ ms) than reported for tagged versions of FUS ($\tau_{mean} = \sim 150$ ms for green fluorescence protein-labeled FUS[39], $\tau_{mean} = \sim 570$ ms for maltose-binding protein-labeled FUS[54]). Taken together, these observations suggest that full-length tag-free FUS forms highly liquid condensates with phase-separation properties distinctive from commonly used truncated or tagged FUS models.

To visualize entire condensates using highly inclined and laminated optical sheet (HILO)[55] microscopy, we doped 10 nM sparsely AlexaFluor488-labeled FUS (FUS-AF488) into the condensation reaction, whereas to perform SMT and measure the intra-condensate diffusion of single biomolecules we added 50 pM fluorescently labeled protein or RNA. Without tethering, we observed that condensates moved laterally on a polyethylene glycol(PEG)-passivated surface (Fig. 1f). In addition, SMT trajectories of mRNA molecules within the same condensate were highly correlated, suggesting a significant contribution from both translational and rotational motions of the entire condensate (Fig. 1g). Previously reported intra-condensate SMT trajectories of relatively small proteins appear to have been less affected[27,28,30-32], suggesting that the comparably slow diffusion of mRNA molecules elevates this challenge. To prevent this interference of condensate motions with intra-condensate SMT observation, we developed a PEG-biotin:streptavidin:FUS-biotin tethering system, wherein the fraction of PEG-biotin controls tether density, and extensive washing prevents the contamination of condensates with streptavidin or FUS-biotin (Fig. 1h). Notably, after optimizing the tether density to avoid surface wetting, we observed surface-captured FUS condensates that were spherical in both the x-y

plane (Fig. 1i, Fig. S3) and the x-z plane (Fig. 1j), rather than the previously reported flattened wetted domains[32-34]. Moreover, the uniform distribution of fluorescence intensity across the bulk fluorescence image of a tethered condensate (Fig. 1i) confirms that our full-length tag-free FUS condensates consisted of a single phase, rather than the multiphase organization of RNP granules assembled using multiple scaffolds[56]. Overall, multi-tethering provides an adaptable platform for accurate SMT within highly liquid-like, single-phase, full-length tag-free FUS condensates (Fig. 1h, #1-3), as exemplified by the uncorrelated mRNA diffusion trajectories in the HILO cross-section imaging plane of an individual condensate (Fig. 1k).

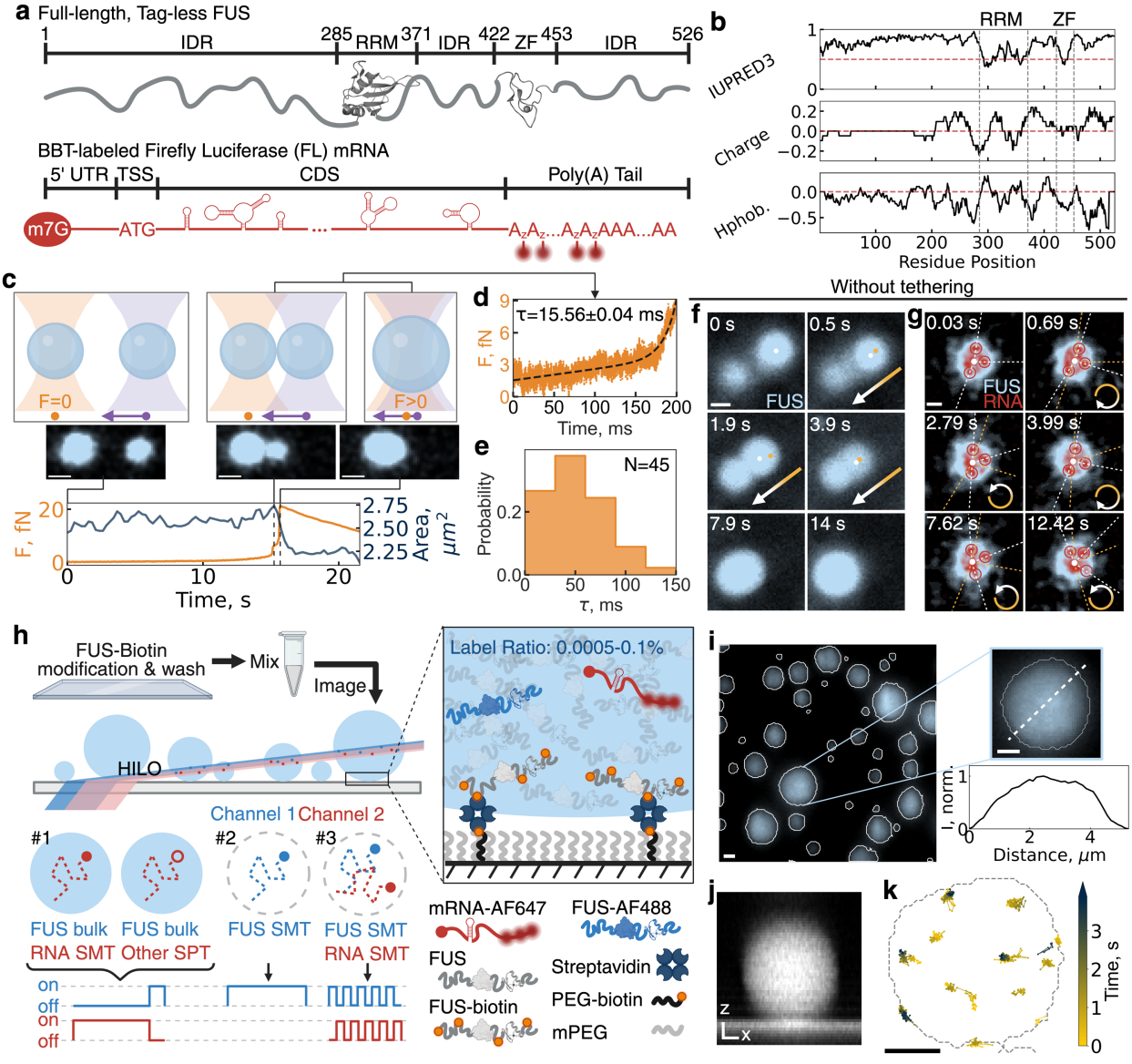

Fig. 1 | Tethering enables accurate single particle tracking of protein and RNA molecules within 3D biomolecular condensates.

a | Schematic of the purified model protein and RNA. **b** | Physicochemical profile of the full length FUS protein. All curves are running window analyses with a window size of 21 residues. IUPRED3 is a prediction score for IDR, curated by experimental database DisProt. Charge density is calculated from each residue's pKa assuming pH=7. Hydropathy (Hphob.) is calculated with hydrophobicity scales determined by Eisenburg et al[57]. The red dotted line indicates the threshold of structured (<0.5) versus unstructured (>0.5), positively versus negatively charged, or hydrophobic (>0) versus hydrophilic (<0). **c** | Schematic of a C-Trap experiment that combines the force measurement from optical tweezers and the condensate total area from scanning-confocal fluorescence microscopy to measure the rheology of full-length, tag-free FUS condensates. **d** | Fitting of the high-frequency force data yields the rate constant τ (characteristic fusion time) of condensate fusion. **e** | Distribution of τ. Measurements were done in three biological replicates with N being the number of condensate pairs measured. **f,g** | Condensates can undergo coalescence (**f**) and translational (arrows in **f**) or rotational (arrows in **g**) motions in the absence of surface tethers. The centroid position of a condensate (**f**) and the angular positions of three RNA molecules (**g**) in the current and previous frame are shown in white and yellow, respectively. **h** | Schematic of a tethered, sparsely labeled condensate system enabling single-molecule and -particle tracking (SMT and SPT) in one or two channels simultaneously within a single biomolecular condensate. #1-3 are three types of experiments to determine the sub-condensate heterogeneity using different probes. For bulk fluorescence imaging of condensates, a labeling ratio < 0.01% was used to minimize the impact of fluorophores on condensates. **i** | Bulk fluorescence image of tethered FUS condensates in a highly inclined laminated optical light sheet (HILO) microscope with the condensate boundary detected by a machine-learning-based pixel classifier, the best method for condensates with a broad range of sizes[58], and the normalized intensity (I, norm.) profile along the white dotted line of the zoomed-in condensate. **j** | Side view of a representative tethered FUS condensate shows its spherical shape. **k** | Representative RNA trajectories within a condensate in a typical video from a type #1 experiment in **h**. The gray dotted line indicates the detected boundary of a tethered FUS condensate from bulk fluorescence. IDR, intrinsically disordered region; RRM, RNA-recognition motif; ZF, zinc-finger domain; BBT, between-body-and-tail labeling strategy for mRNA; UTR, untranslated region; TSS, translation start site; CDS, coding sequence; ALEX, alternating-laser excitation; PEG, polyethylene glycol; mPEG, PEG monomethyl ether. All scale bars are 1 μm.

Nanodomains govern intra-condensate diffusion patterns

To systematically profile heterogeneous intra-condensate diffusion behaviors (Fig. 2a), we developed a pipeline that categorizes SMT trajectories by diffusion type (Fig. 2a-b) and assesses population-wide shifts via distributions of specific observed metrics (Fig. 2c). Generally, in the absence of active transport SMT trajectories can be assigned to one of three diffusion types: immobile, confined diffusion, and normal diffusion (Fig. 2a), which are distinguished by the mean step size of a trajectory and the anomalous diffusion component α calculated from fitting the trajectory's mean squared displacement (MSD)-lag time (τ) (Fig. 2a-b). Immobile trajectories have step sizes smaller or similar to the mean localization error (Fig. S4) so that a 30 nm threshold was used to distinguish mobile from immobile trajectories (Fig. 2b). For mobile trajectories, confined diffusion yields $\alpha<1$ while normal diffusion ideally exhibits $\alpha=1$. Since α is usually underestimated when fitting experimental data[59], a more practical threshold of 0.7 was used instead of 1 to distinguish normal from confined diffusion trajectories (Fig. 2b). The α estimates from single trajectories followed a broad distribution (Fig. 2c) so that we used the distribution of angles between steps calculated from all trajectories (Fig. 2c) as an orthogonal metric to quantify how significantly molecules were confined. An angle distribution

skewing towards 180° is expected for confined particles because they bounce back when approaching their confinement boundary, where 0° is defined as no change in directionality and 180° as a complete turn-back. In contrast, a uniform angle distribution is expected for normal diffusion, due to its isotropic nature. For normal diffusion trajectories, we used both MSD-τ fitting (Fig. S5) and a Bayesian statistics-based state array (SA) method[60] (Fig. 2c) to estimate the distribution of apparent diffusion coefficients (D_{app}). To test the resulting diffusion-profiling pipeline, we used 20-nm and 200-nm polystyrene beads in the dilute phase outside of condensates as a normal diffusion control. We confirmed signatures of normal diffusion in both of these controls, with a normal diffusion fraction of 65-76%, an α distribution peak at 1, a uniform angle distribution, and single sharp peaks in the D_{app} distribution. As expected from the Stokes-Einstein diffusion law, the peak for the 20-nm beads was shifted from that of the 200-nm beads roughly by a factor of 10 (Fig. S6, Table S1). Notably, the diffusion profile of single FL mRNA molecules in the dilute phase matched well with that of the 20-nm beads (Fig. 2c, Fig. S6), further validating our pipeline because the radius of gyration for such a 1500-nt RNA was previously determined to be ~20 nm[61]. Collectively, these results indicate that our pipeline is well suited to categorize diffusion behaviors within an SMT dataset.

To assess the diffusion of both protein scaffold and RNA guest molecules inside condensates, we applied our pipeline to the corresponding SMT datasets (Fig. 2b-c, Fig. 1h #1-2). Previous studies have observed multiple normal diffusion states of protein scaffold molecules within membrane-wetted domains or non-tethered 3D condensates with a D_{app} ranging from ~0.01 to ~0.52 $\mu m^2/s$[27,30-32]. Similarly, we found multiple diffusive states of FUS within the normal diffusion fraction, with a dominant peak at 0.81 $\mu m^2/s$ (Fig. 2c, Table S1). Remarkably, we additionally found that both intra-condensate FUS and mRNA molecules were significantly confined, with confined fractions of 67 ± 1% and 83 ± 2%, respectively, considerably higher than that of the outside dilute phase mRNA control (40 ± 2%; Fig. 2b). Confined diffusion was further supported by an α component distribution biased toward 0 and an angle distribution skewing toward 180° (Fig. 2c, Table S1). The D_{app} distributions of unconfined FUS and mRNA molecules were partially overlapping, suggesting the formation of RNP complexes, whereas a fast-diffusing peak was found only in the FUS distribution, consistent with the relatively small molecular weight of the free protein (Fig. 2c). The diffusion of unconfined mRNA molecules within condensates was slower than that of mRNA outside of condensates, which suggests an elevated viscosity in the condensed phase but cannot explain the confined diffusion. Collectively, these findings revealed that both FUS scaffold and mRNA guest molecules are significantly confined within a condensate, with mRNA more confined than FUS, while the normal diffusion fraction contains multiple diffusive states, some of which may represent RNP complexes.

To probe the spatial relationship between the confinement of scaffold and guest molecules, we next sought to visualize the sub-condensate architectures that dampen diffusion . To this end, we performed point accumulation for imaging in nanoscale topology (PAINT)[6] reconstruction from SMT trajectories, termed SMT-PAINT (Fig. 2d), using dual-color SMT under alternating laser excitation (ALEX) to avoid bleed-through artifacts (Fig. 1h #3). In a SMT-PAINT image, unconfined and fast-moving molecules leave fewer point locations and thus less pixel intensity than confined molecules because they quickly exit the imaging plane due to axial diffusion under HILO microscopy. Only confined molecules will significantly increase local point density and result in bright puncta in an SMT-PAINT image. We also ensured sufficient coverage of locations within a condensate by introducing an oxygen scavenging system (OSS) that extended SMT video length from the previous ~200 frames (4 s) to ~10,000 frames (200 s) (Fig. 2d, Fig. S7). The concentration-dependent increase observed in the number of trackable particles supports that the trajectories used for SMT-PAINT arose from the titrated molecules of

interest (Fig. S7). Using SMT-PAINT, we found distinct nanometer-scale regions that confine FUS and mRNA, which we term nanodomains (Fig. 2e). The negative mean pixel-wise Pearson correlation coefficient (PCC) between the two nanodomains was -0.26 ± 0.02, suggesting a slight exclusion effect (Fig. 2f). To further assess how non-confined molecules distribute throughout a condensate, we used step size heatmaps to measure the spatial distribution of fast-diffusing molecules (Fig. 2g). We found that fast-diffusing FUS and mRNA molecules were spatially correlated with a positive mean PCC of 0.42 ± 0.02 (Fig. 2h), suggesting co-diffusion of FUS and mRNA that was further supported by cross-pair correlation function (G_{cross}) (Fig. S8). Taken together, these results yield intra-condensate diffusion patterns where distinct nanodomains confine protein scaffold and RNA guest molecules, while fast-diffusing molecules generally colocalize outside of these nanodomains.

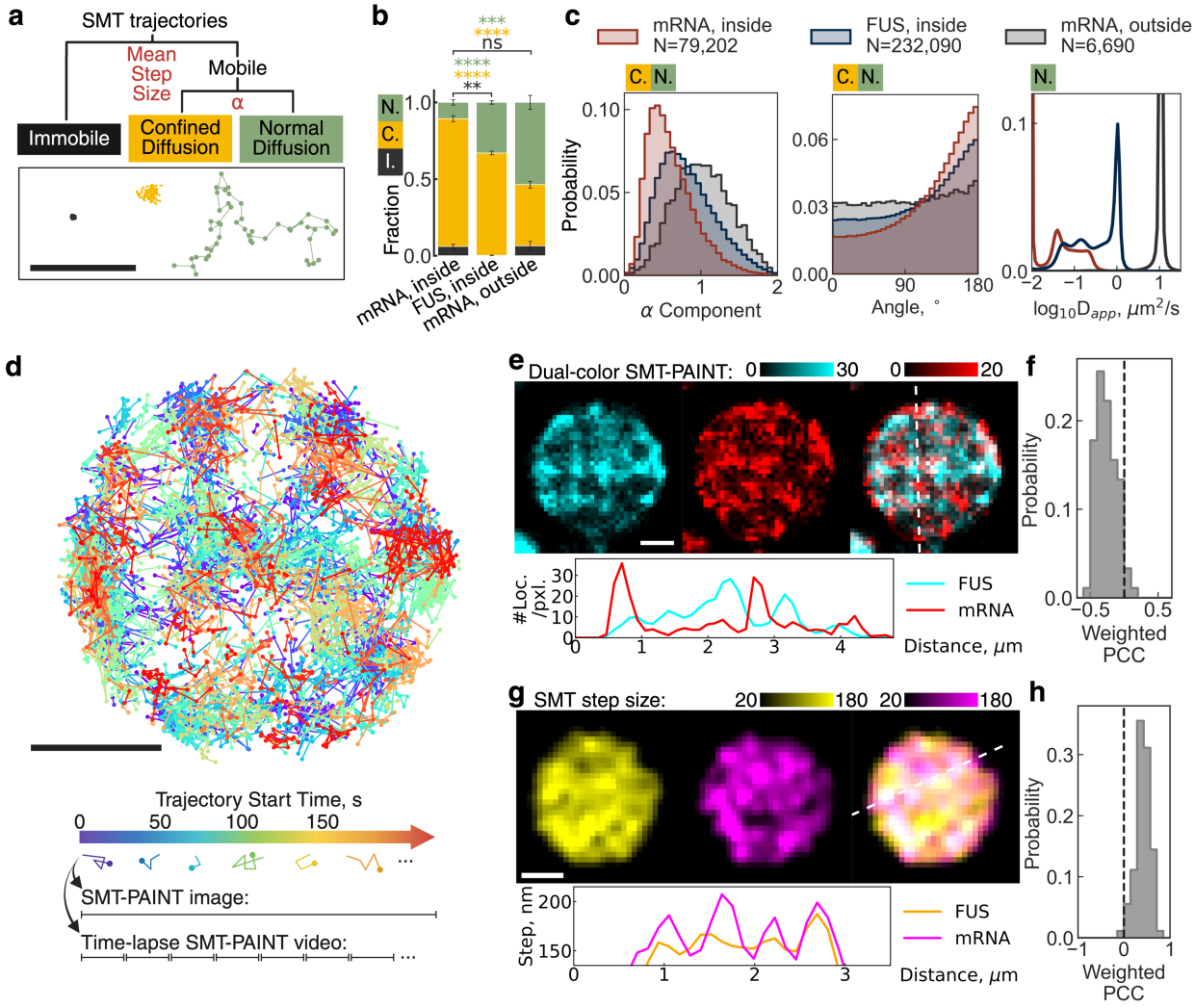

Fig. 2 | FUS and RNA are confined in nanodomains.

a | Three representative mRNA trajectories within a single full-length tag-free FUS condensate, which can be classified into three categories: immobile, confined diffusion, and normal diffusion. **b** | Fractions of three categories for mRNA and FUS molecules in the condensed phase, and for mRNA

molecules in the dilute phase. Error bars are SEM from at least three experiments on different days. **c |** Distributions of diffusion metrics, including the anomalous diffusion component α, the angle between adjacent steps, and the apparent diffusion coefficient (D_{app}). Total number of molecules N in each dataset is included in the legend. The colored boxes on the top left corner of each distribution indicate the diffusion type(s) of molecules included in the plot. The α distribution was derived from mobile molecules with an R^2>0.7 in MSD-τ fitting. The angle distribution was calculated from all molecules. The D_{app} distribution was calculated from normal diffusion molecules only. The D_{app} distribution was calculated via a state array (SA) method[60]. **d |** Raw SMT trajectories of FUS molecules within a single condensate and schematic for two ways of SMT-PAINT reconstruction. A plot of all FUS trajectories in a representative tethered condensate, colored by the start time of each trajectory. An SMT-PAINT image was generated by accumulating locations of all trajectories throughout a SMT dataset. Each frame of a time-lapse SMT-PAINT video was reconstructed by accumulating locations of trajectories within a time windows that is non-overlapping with adjacent windows. **e** | Dual-color SMT-PAINT of FUS and mRNA with a cross-sectioning profile along the white dotted line. Pixel intensity represents the number of SMT trajectories in each pixel. **f |** Distribution of pixel-wise Pearson Correlation Coefficient (PCC) of **e**, weighted by the number of SMT trajectories per pixel. A gray dotted line indicates PCC=0, distinguishing positive correlation (PCC>0) and negative correlation (PCC<0). **g |** A heatmap of average step size of all FUS or mRNA trajectories on top of each pixel, with a cross-sectioning profile along the white dotted line. The higher the pixel intensity, the higher the average step size, or faster the diffusion. **h |** Pixel-wise weighted PCC of **g**. All scale bars are 1 μm. Statistics annotation: independent t-test, ns: 0.05 < p <= 1, *: 0.01 < p <= 0.05, **: 0.001 < p <= 0.01, ***: 0.0001 < p <= 0.001, ****: p <= 0.0001.

Functional impact of nanodomains on FUS and RNA

To gain deeper insight into the impact of nanodomains on the internal environment within a condensate, we first characterized the mobility of FUS nanodomains by time-lapse SMT-PAINT, where subsets of SMT trajectories within non-overlapping time windows were reconstructed into frames of a video (Fig. 2d, Fig, 3a). The motion of FUS nanodomains was determined to be slower than 10 nm/s based on the mean step size of nanodomains in these time-lapse videos, which was smaller than our localization errors (Fig. S4). Therefore, FUS nanodomains as a whole are immobile at the minute timescale relative to the condensate. To explore the influence of nanodomains on the local chemical environment within a condensate, we performed fluorescence lifetime imaging (FLIM) on 10 nM AlexaFluo488-labeled FUS within tethered condensates (Fig. 3b), where changes in fluorescence lifetime reflect an altered chemical environment[62] around the AlexaFluo488 dye. FLIM images showed nanometer-scale regions of low and high lifetime inside a condensate, with a minimum of ~3.2 ns and a maximum of ~3.5 ns, and a much higher lifetime of ~5.7 ns in the dilute phase (Fig. 3b). Since our FLIM images were averaged from 10 scans spanning across ~5 min, any difference in lifetime associated with fast moving intra-condensate regions would have blurred out due to averaging. Therefore, we reasoned that the ~0.3 ns dispersion of lifetimes within a condensate is caused by a relatively immobile intra-condensate architecture, in particular the extremely slow-moving nanodomains (Fig. 3a). To further test this hypothesis, we performed a fluorescence correlation spectroscopy (FCS) analysis at ten random locations within each tethered condensate on the same time-resolved confocal microscope used for FLIM to simultaneously derive local D_{app} values and fluorescence lifetime (Fig. 3c). The ten random locations are expected to sample both nanodomains and the spaces around them for us to relate local fluorescence lifetime and nanodomain-induced changes in D_{app}, although FCS cannot distinguish slow from confined

diffusion. Indeed, we observed a positive correlation between lifetime and D_{app} (Fig. 3c), suggesting that the ~0.3 ns decrease of lifetime in FLIM images was caused by FUS nanodomains of low D_{app}. Finally, we tested another previously used method to probe the intra-condensate chemical environment – imaging with Nile Red[26,28]. Although we found bright Nile Red puncta near the condensate surface, control experiments found such puncta also in the absence of condensates, indicating that they were caused by aggregation at the previously used dye concentrations, rather than an altered chemical environment (Fig. S9). Taken together, FUS nanodomains represent a slow-moving sub-condensate architecture that provides a distinct local chemical environment.

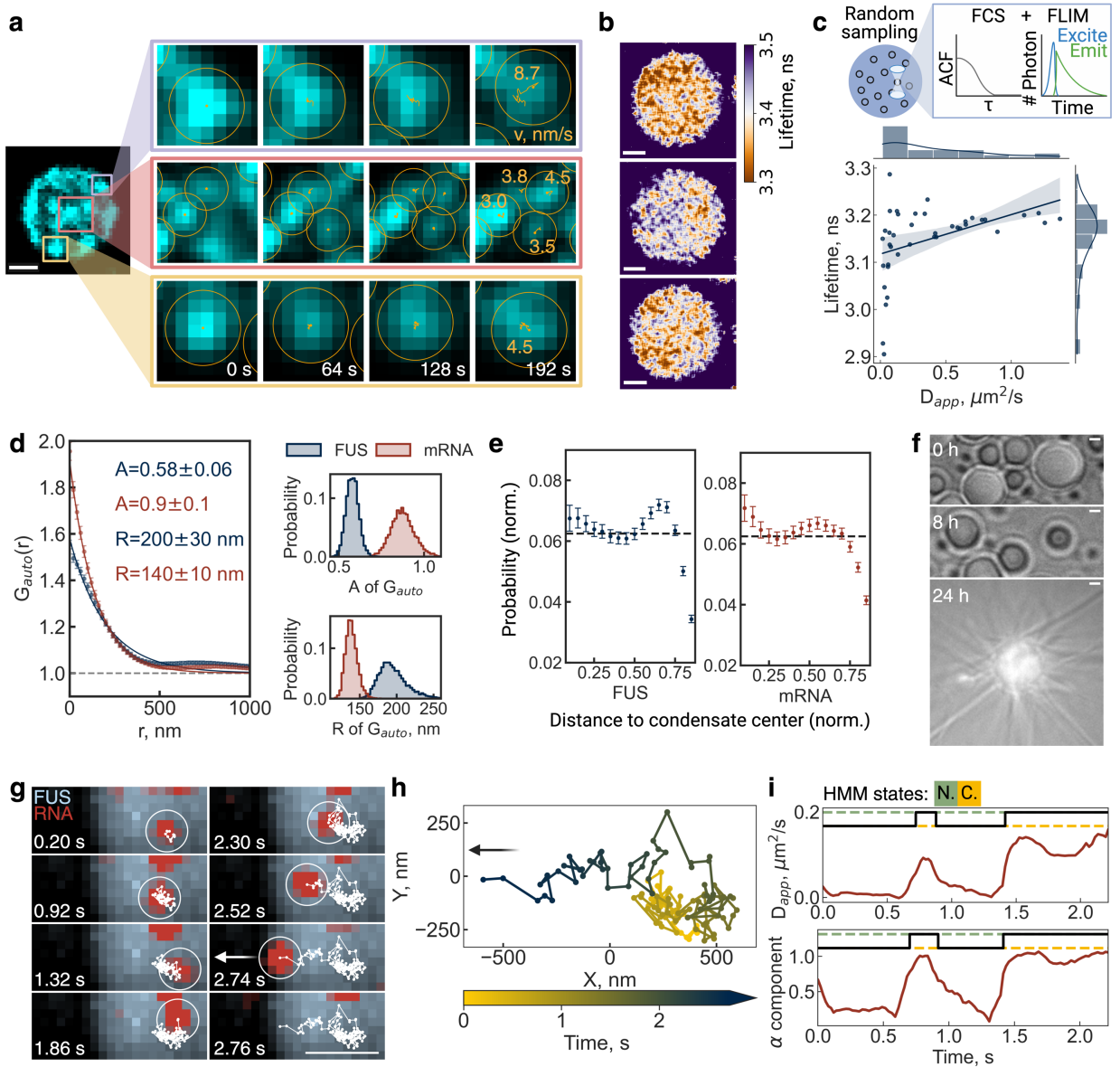

Fig. 3 | Nanodomain properties and their functional impacts on FUS and RNA.

a | Time-lapse SMT-PAINT reconstructions of nano-domains that confine FUS motions in the zoomed-in regions labeled by three different colored boxes in a SMT-PAINT image. Motions of the underlying nanodomains are depicted by orange trajectories, annotated with the velocity calculated from the mean step size of each trajectory. **b |** Fluorescence lifetime imaging microscopy (FLIM) of AlexaFluo488-labeled FUS. **c |** Cartoon and results of a random-sampling fluorescence correlation spectroscopy (FCS)-FLIM assay on a time-resolved laser-scanning confocal microscope. The scatter plot shows the correlation between D_{app} measured by FCS and lifetime by FLIM with the distributions of each on the respective side. The blue line shows a linear regression model fit with the shaded area being the 95% confidence interval of the fit. **d |** Auto-pair correlation function (G_{auto}) of FUS or mRNA single-molecule locations, with amplitude (A) and radius (R) extracted by fitting with an exponential decay with a baseline of 1. A gray dotted line indicates $G_{auto}=1$, demarcating a random distribution without clustering ($G_{auto}>1$) or self-exclusion ($G_{auto}<1$). 95% confidence intervals of A and R were calculated by parametric bootstrapping, while the fitting results from each bootstrap are shown as histograms. Error bars are SEM of G_{auto} across different condensates, weighted by the number of SMT trajectories in each condensate. **e |** Distribution of FUS and mRNA nanodomains relative to the center of each condensate. The distance to condensate center is normalized by the size of the condensate, while the probability is normalized by the molecular density and the increasing ring area from center to periphery of a condensate. Gray dotted lines indicate an expected uniform distribution of molecules, randomly distributed throughout each condensate. Error bars are 95% confidence interval determined by non-parametric bootstrapping. **f |** Bright-field images of FUS fibril out-growth from the condensate surface after 24 hours incubation at room temperature. **g |** Exemplary multi-stage diffusion trajectory of an mRNA moving from one confined region to another, followed by normal diffusion until the mRNA leaves the FUS condensate from the edge. The white circle indicates the current position of the mRNA, while the white line indicates the trajectory before the current frame. **h |** A zoomed-in view of the trajectory, colored by the time each location is detected. **i |** Running-window analysis of D_{app} and α value from a window size of 20 steps. Hidden Markov Model (HMM) is used to determine the transition point between confined and normal diffusion states. All scale bars are 1 μm. Statistics annotation: independent t-test, ns: $0.05 < p <= 1$, *: $0.01 < p <= 0.05$, **: $0.001 < p <= 0.01$, ***: $0.0001 < p <= 0.001$, ****: $p <= 0.0001$.

Since the 50 pM mRNA guest concentration was negligible relative to the 10 μM total concentration for FUS scaffold, we reasoned that nanodomains confining mRNAs are specialized FUS nanodomains that confine mRNA molecules, and asked how different the two types of nanodomains are in size, confinement strength, and relative location within the condensate. For brevity and clarity, we will use the following abbreviations throughout the remainder of this article: FUS nanodomains for nanodomains that predominantly confine FUS molecules, and RNA nanodomains for nanodomains that confine FUS less but more strongly RNA molecules. First, we calculated the auto-pair correlation function (G_{auto}) of all locations from FUS or mRNA SMT trajectories to determine the size and ability to retain molecules of FUS nanodomains and mRNA nanodomains, as the radius (R) and amplitude (A) of G_{auto}, respectively (Fig. 3d). The radius of FUS nanodomains was determined to be 190 ± 30 nm while mRNA nanodomains are 130 ± 10 nm (Fig. 3d). FUS molecules were 58 ± 6% more likely to be confined in FUS nanodomains compared to randomly distributed within a condensate, while mRNA molecules were 90 ± 10% more likely to be confined in mRNA nanodomains (Fig. 3d). In line with the modest probability increase in FUS compared to mRNA nanodomains, fast-moving FUS molecules also transitioned through the FUS nanodomains, whereas fast-moving mRNA molecules were mostly excluded from the RNA nanodomains (Fig. S10). That is, FUS nanodomains have a weaker ability to retain molecules and are of bigger size than mRNA

nanodomains. Second, we calculated the normalized location distribution of both nanodomains relative to the condensate center and found distinct distribution patterns (Fig. 3e). FUS nanodomains predominantly localize to the peripheral region of a condensate, evidenced by a 15 ± 3% increase in probability compared to a random distribution, with a more minor preference for the center of a condensate, observed as an 8 ± 7% increase (Fig. 3e). In contrast, mRNA nanodomains predominantly locate to the condensate center (15 ± 7% increase in probability), and less locate to the periphery (7 ± 3% increase; Fig. 3e). Remarkably, the peripheral localization of FUS nanodomains, observed here right after condensate assembly, coincides with surface-originating fibril out-growth after 24 hours, a phenomenon associated with condensate aging[39,63] (Fig. 3f). These findings suggest that FUS nanodomains may facilitate the recently reported surface-induced liquid-to-solid transition of FUS[28,63,64]. In summary, FUS nanodomains are distinct from mRNA nanodomains in size, confinement strength, and location within a condensate, which may contribute a distinct chemical environment that primes the fibrilization of FUS from the surface of a condensate.

Given that the mRNA nanodomain is a specialized but distinct version of a FUS nanodomain, we hypothesized that it may play a role in regulating RNA residence time in a condensate by trapping. Indeed, the escape path of an mRNA molecule from the inside to the outside of a condensate was significantly prolonged by the presence of mRNA nanodomains (Fig. 3g-i). As shown in a representative trajectory (Fig. 3g-h), an mRNA molecule was initially confined within a nanodomain from 0 to 0.92 s. Following escape from the first nanodomain, it became trapped in a second nanodomain until 1.86 s. After a second escape, the mRNA molecule diffused freely and reached the condensate boundary at 2.74 s, at which point it disappeared from the focal plane due to rapid axial diffusion in the dilute phase. To confirm that the extended escape time was due to confinement within two mRNA nanodomains rather than dampened diffusion by an increased local viscosity, we implemented a running-window analysis of D_{app} and the α component of the trajectory and found clear transitions between normal and confined diffusion states (Fig. 3i). In contrast to the potential role of FUS nanodomains in condensate aging, nanodomain-induced confined diffusion of mRNA molecules was only marginally promoted by aging (Fig. S11). To test whether an excess of RNA can rescue mRNA molecules from nanodomains via competitive binding, we added 50 ng/μL Hela cell total RNA during the reconstitution of condensates and profiled the diffusion of mRNA molecules within condensates (Fig. S12). We found only a marginal change in the fraction of confined diffusion mRNA molecules but the disappearance of a slower diffusive state in the normal diffusion fraction (Fig. S12). This suggested that the addition of total RNA indeed rescues some mRNA molecules from protein binding, but it only affects freely diffusive mRNA molecules with no impact on nanodomain-induced confinement. In summary, mRNA nanodomains mainly function as traps that increase mRNA residence time in condensates, independent of condensate aging or the presence of an excess amount of RNA background.

Size, shape, and charge determine intra-condensate diffusion

We next asked how the properties of a biomolecule, such as size, shape and charge, affect their intra-condensate diffusion profile. Specifically, we probed why mRNA as a highly negatively charged, high-molecular-weight molecule was more confined in nanodomains than FUS, a mixed-charge, comparably lower molecular weight molecule (Fig. 3d, Fig. 1b). Previous studies have reported a preference for some RNP granules to recruit longer RNAs[65-67]. Based on this knowledge, we first examined whether the confinement of RNA molecules in nanodomains is affected by length, by comparing the 1500-nt long FL mRNA with a 22-nt short microRNA (miRNA; here miRNA21) by using dual-color tracking (Fig. 4a-c, using Fig. 1h #3).

SMT-PAINT images showed that miRNA molecules had a more diffusive distribution (Fig. 4a) than mRNA (Fig. 2e). Analysis with G_{auto} further revealed that miRNA molecules were only 30 ± 3% more likely to be confined in condensate nanodomains than expected for a random distribution (Fig. 4b, Fig. S13), significantly lower than the 90 ± 10% increase in probability for mRNA (Fig. 3d). Moreover, the 220 ± 30 nm radius of miRNA nanodomain uncovered by G_{auto} (Fig. 4b, Fig. S13) far exceeded the 130 ± 10 nm radius of mRNA nanodomain (Fig. 3d). The nearly-zero mean PCC of -0.05 ± 0.02 in FUS-miRNA SMT-PAINT images further revealed a weaker exclusion effect between FUS and RNA nanodomains than those of FUS and mRNA (Fig. 4c). These modestly confining, large miRNA nanodomains explain the more diffusive pattern of miRNA in SMT-PAINT images (Fig. 4a). Notably, a consistent intra-condensate diffusion pattern was observed, namely a strong co-localizing effect on fast-diffusing protein and RNA molecules, with weak exclusion of confined protein and RNA molecules (Fig. 4c, Fig. S8). Given the weak nature of these miRNA nanodomains, we next tested whether the single Cy5 dye on the miRNA itself exerts an influence on diffusion, by testing the free dye (Fig. 4d-e, using Fig. 1h #1). Unlike the expected slower normal diffusion when decreasing the molecular weight from RNA to free dye (Fig. 4e D_{app} spectrum), Cy5 is more confined than miRNA molecules, with a 53 ± 1% confined fraction that is slightly larger than the 46 ± 2% of the miRNA (Fig. 4d). This conclusion is also supported by the α and angle distributions (Fig. 4e, Table S1). These observations indicate that the confinement of the Cy5-labeled miRNA was likely the base line of confinement observable within a condensate, possibly due to non-specific dye-protein interactions[68]. To conclude, only long RNAs like mRNAs, but not short RNAs like miRNAs, are significantly confined within nanodomains.

We further investigated how other physicochemical properties of mRNA, such as overall size, shape and strong negative charge of the ribose-phosphate backbone, contribute to intra-condensate diffusion. To this end, we compared the intra-condensate diffusion profiles of FL mRNA molecules and carboxylate-modified 20-nm beads, which mimic the charge and ~20 nm gyration radius of a typical 1,500-nt mRNA[61] (Fig. 4f-g). Compared to the linear-polymer mRNA molecules, the spherical beads have a higher immobile fraction in condensates (Fig. 4f). This finding aligns with the fact that elongated, but not globular-shaped, objects can thread through a meshwork-like environment[69], as found in a condensed, percolated droplet. Such a threading ability of linear mRNA may also explain the slightly faster diffusion among the normal diffusion mRNA fraction compared to the spherical beads (Fig. 4g). To additionally probe the effects of surface charge, we performed SPT on a series of 9.5-nm quantum dots (QD) with negative-charge carboxylate, charge-neutral PEG, and positive-charge amine coated surfaces (Fig. 4h-i). Notably, all aspects of the diffusion profile remain the same between negatively and positively charged QDs, including fractions of diffusion type (Fig. 4h) and the distributions of α component, angle, and D_{app} (Fig. 4i). The only difference among QDs was that the neutral QDs had a larger immobile fraction than either of the charged QDs (Fig. 4h). Taken together, unlike the length of an RNA, which determines confinement in nanodomains, both the linear-polymer nature and negative charge of an mRNA primarily contribute to maintaining its mobility in condensates but do not govern its confinement.

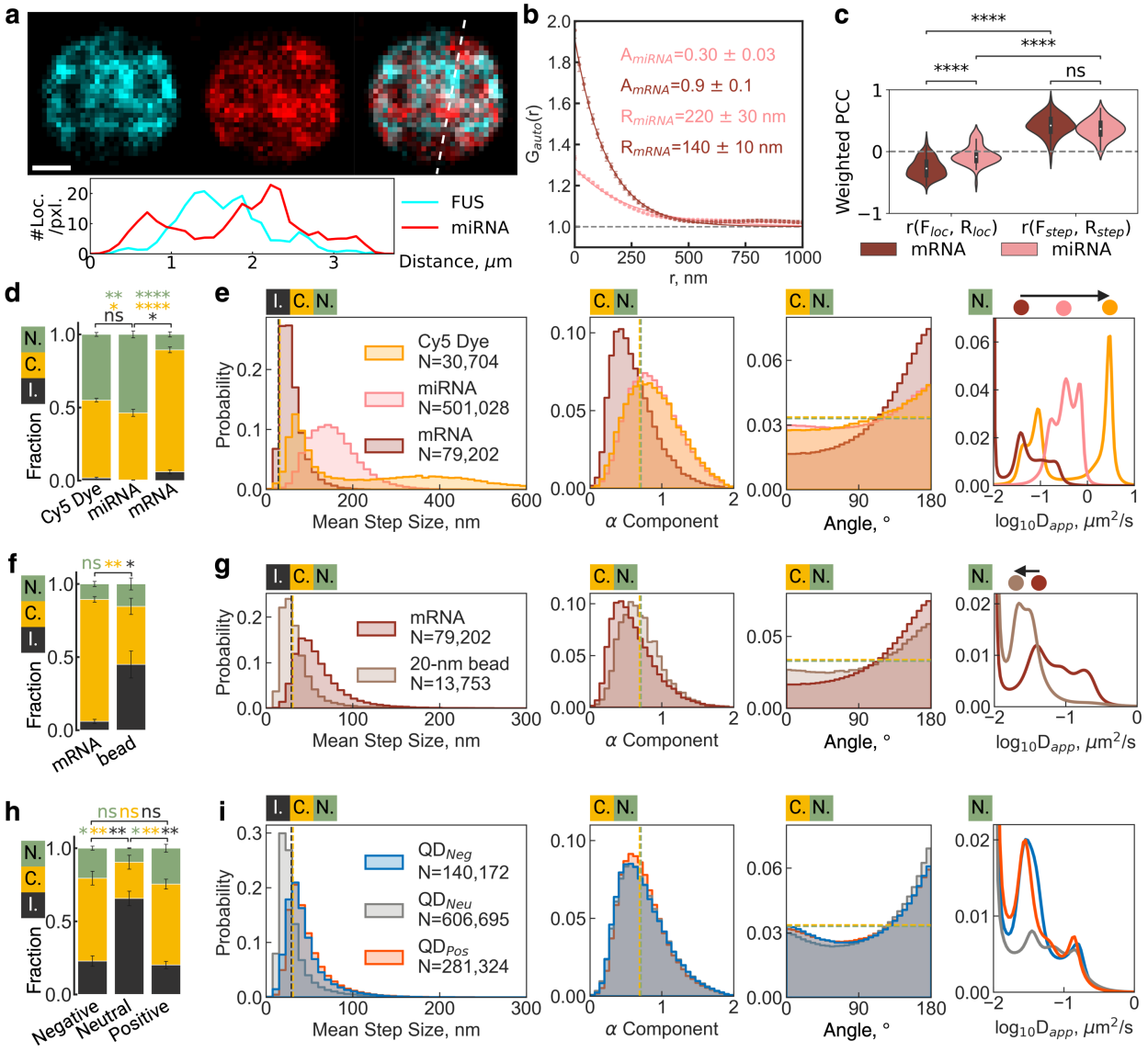

Fig. 4 | Effect of size, shape, and charge on the intra-condensate diffusion profile.

a | Dual-color SMT-PAINT of FUS and micro-RNA (miRNA) with a cross-sectioning profile across the white dotted line. Pixel intensity represents the location density on each pixel. **b** | Auto-pair correlation function (G_{auto}) of FUS or miRNA single-molecule locations, with amplitude (A) and radius (R) extracted by fitting to an exponential decay with a baseline of 1. A gray dotted line indicates G_{auto}=1, suggesting random distribution without clustering (G_{auto}>1) or self-exclusion (G_{auto}<1). 95% confidence intervals of A and R were calculated by parametric bootstrapping. Error bars are SEM of G_{auto} across different condensates, weighted by the number of SMT trajectories in each condensate. **c** | Pixel-wise weighted PCC of dual-color SMT-PAINT images of FUS and mRNA or miRNA, abbreviated as r(F_{loc}, R_{loc}), and of average step size images, abbreviated as r(F_{step}, R_{step}). A gray dotted line indicates PCC=0, distinguishing positive correlation (PCC>0) and negative correlation (PCC<0). **d, f, h** | Fractions of the immobile (I.), confined diffusion (C.) and normal diffusion (N.) categories for mRNA, miRNA, and free Cy5 dye molecules in the condensed phase (**d**), mRNA molecules and 20-nm carboxylate-modified beads in the condensed phase (**f**), and amine-,

PEG-, carboxylate-functionalized quantum dots (QDs) in the condensed phase (**h**). Error bars are S.E.M. from more than three experiments on different dates. **e, g, i |** Distributions of the mean step size of each trajectory, the anomalous diffusion component α, the angle between adjacent steps, and the apparent diffusion coefficient (D_{app}) for mRNA, miRNA, and free Cy5 dye molecules in the condensed phase (**e**), mRNA molecules and 20-nm carboxylate-modified beads in the condensed phase (**g**), and amine-, PEG-, carboxylate-functionalized quantum dots (QDs) in the condensed phase (**i**). The colored boxes in the top left corner of each distribution indicate the diffusion type(s) of the molecules included in the plot. The mean step size distribution is from all molecules, and the total number of molecules N is included in the legend. The α and angle distributions are from all mobile molecules or particles while the D_{app} distribution is from only normal diffusion molecules or particles. The D_{app} distribution is calculated by a state array (SA) method, while the D_{app} distribution calculated by mean squared displacement (MSD)-τ fitting can be found in Fig. S5. The D_{app} distribution is scaled to visualize the smaller peaks. A double-layered black-yellow dotted line indicates the threshold between immobile (black) and confined diffusion (yellow) diffusion, while a double-layered yellow-green dotted line indicates the threshold between confined (yellow) and normal (green) diffusion. All scale bars are 1 μm. Statistics annotation: independent t-test, ns: $0.05 < p <= 1$, *: $0.01 < p <= 0.05$, **: $0.001 < p <= 0.01$, ***: $0.0001 < p <= 0.001$, ****: $p <= 0.0001$.

Discussion

Intra-condensate heterogeneity caused by a multiphase architecture, such as observed in the nucleolus, has long been characterized[56,70], but intra-condensate heterogeneity independent of a secondary phase transition was only recently reported[26,28,63,71]. Percolation, a connectivity transition to form a network of physical bonds[7], has been found to play a role in the pre-condensation assembly of protein clusters below the saturation concentration[72], and of protein-RNA condensates after assembly[73,74]. However, it has remained unclear whether percolation has to be global, spanning throughout the condensate, or can be local. Our work addresses this question by characterizing nanodomains, which exemplify a local, rather than global, percolation emerging in liquid condensates assembled from full-length, tag-free FUS. Nanodomains revealed by SMT-PAINT confine either FUS scaffold molecules or RNA guest molecules (Fig. 2). Yet, they do not increase molecular density since they do not appear in bulk fluorescence images (Fig. 1i,j), where a secondary phase separation would lead to changes in local concentration detectable in the fluorescence signal. Given that 99.9995% of molecules in our condensate represent FUS, a model emerges in which the nanodomains confining FUS and those confining RNA are both formed by local percolation of FUS, but at distinct levels of local connectivity, possibly due to different FUS conformations (Fig. 5). In FUS nanodomains, the higher connectivity of FUS is sufficient to confine the protein but prevents the larger RNA molecules from entering due to the small pore size of the meshwork. In RNA nanodomains, the comparatively modest connectivity among FUS molecules permits RNA molecules to enter and become confined. As large biopolymers, their high multivalency effectively integrates them into an otherwise dynamic FUS connectivity network. The intra-condensate space outside both types of nanodomains has the lowest connectivity among FUS and thus fast-diffusing FUS and RNA molecules co-localize there (Fig. 5).

The discovery of nanodomains brings to light a previously unexplored dimension of control over the molecular residence time within condensates—by modulating confined diffusion (Fig. 3g-i)—presenting a stark departure from the regulation based on normal diffusion as traditionally proposed[27,29-32]. The quantity, size, and confinement strength of nanodomains can

all affect the escape path and timing of a molecule from a condensate. A molecule will take longer to escape a condensate in the presence of more, larger, and higher connectivity nanodomains (Fig. 5).

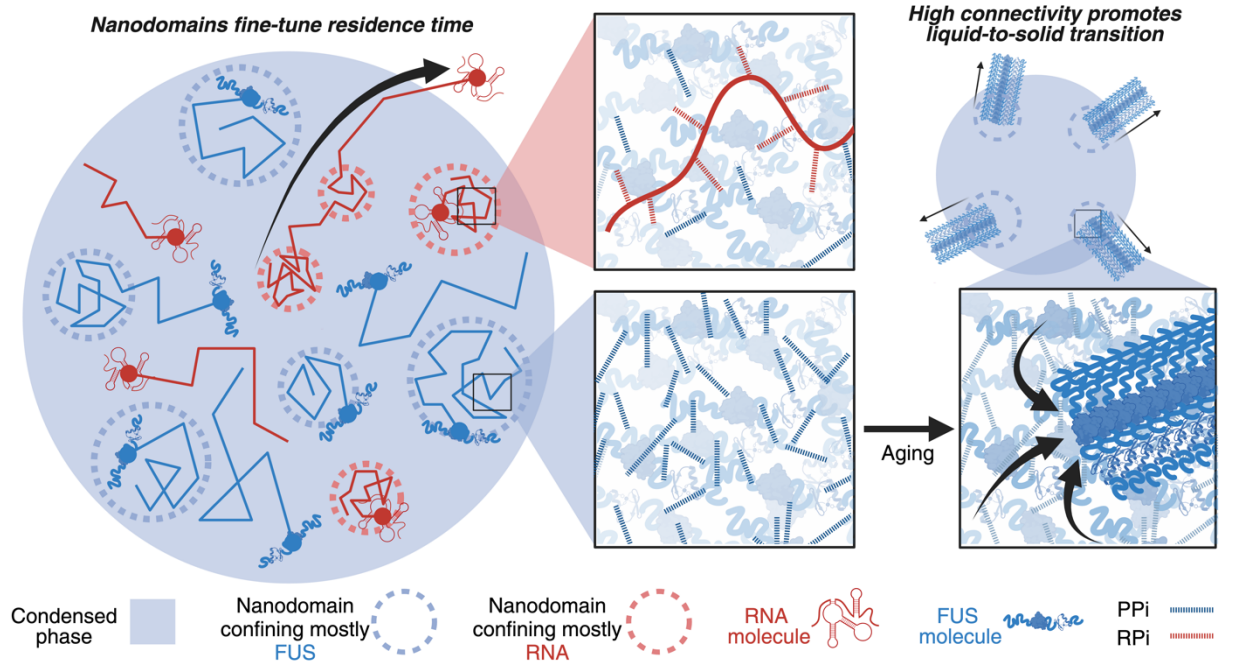

Fig. 5 | Nanodomains govern diffusion within a biomolecular condensate and affect the fate of both protein scaffold and RNA guest molecules.

Given that inter-chain interactions promote aggregation or fibrilization[75], the high local connectivity within FUS nanodomains likely provides a chemical environment (Fig. 3b-c) that would be favorable to stacking between FUS molecules and to fibril growth. We observe nanodomains to form shortly after condensate assembly, often near the condensate periphery (Fig. 3e), so that they could prime the fibrilization of FUS during later condensate aging, explaining the surface-originating FUS fibril out-growth characterized in both previous studies[28,63,64] and our work (Fig. 3f). Therefore, nanodomain-driven, locally tuned, inter-molecular dynamics in condensates may have pathological consequences, complementing a recent report that intra-molecular structural dynamics in condensates remains as fast as in dilute solution[29].

In conclusion, this work represents a significant step forward in identifying the spatiotemporal organization of the internal space of a condensate by demonstrating how nanodomains govern the intra-condensate diffusion profile. The techniques employed here can readily be adapted for other RNP condensates to dissect how they regulate RNA fate. While future work is needed to fully understand the driving forces behind nanodomain formation and their implications for cellular processes, our findings lay the foundation to study sub-condensate regulation of molecular function, en route to a complete understanding of the biophysical basis of condensate function in physiology and disease.

Methods

Purification and labeling of FUS and RNA

Full-length tag-free human FUS was purified following a recently developed protocol[46,47] with a series of ion-exchange chromatography under denaturing condition (Fig. S1), followed by a slow two-step refolding into a storage buffer containing β-cyclodextran (BCD) that prevents phase separation. FUS was over-expressed in E. coli BL21(DE3) from pET-FUS plasmid, a generous gift from the Ishihama group. Culture was grown to OD600=1.0 at 37 °C and induced with 1 mM isopropyl β-D-1-thiogalactopyranoside (IPTG). After 6 h of growth at 37 °C, cells were harvested by centrifugation and suspended with buffer A, 10 % glycerol, 20 mM [4-(2-hydroxyethyl)-1-piperazineethanesulfonic acid] (HEPES)-NaOH pH 7.0, 300mM NaCl, 1 mM dithiothreitol (DTT), 1 mM ethylenediaminetetraacetic acid (EDTA), 0.1 % Tween-20, and 1x cOmplete protease inhibitor cocktail (Millipore Sigma), and store for 30 minutes on ice. Cell lysate was sonicated on ice, and insoluble protein was collected by centrifugation. The pellet was solubilized in a buffer B, 6 M Urea, 10 % glycerol, 20 mM HEPES-NaOH pH 7.0, 1 mM DTT, 1 mM EDTA, and 1x cOmplete protease inhibitor cocktail (Millipore Sigma). After centrifugation, supernatant was filtered with 0.45 μm filter (Fisher) and loaded to HiTrap Q column (Cytiva) on an NGC Fast Protein Liquid Chromatography (FPLC) station (Bio-Rad). The flow-through fraction was mixed with CM Sepharose FF resin (GE HealthCare Lifesciences) on a rotator at 4 °C over night and passed through an open column to remove resin. The flow-through fraction was loaded to HiTrap Capto S column (Cytiva) on NGC FPLC station. The flow-through fraction was loaded to HiTrap SP HP column (Cytiva) on NGC FPLC station, and bound proteins were fractionated with 0 to 500 mM linear gradient of NaCl in buffer C, 6 M Urea, 10 % glycerol, 20 mM HEPES-NaOH pH 7.0, 1 mM DTT and 1 mM EDTA. FUS fractions were examined on sodium dodecyl sulfate (SDS) - polyacrylamide gel electrophoresis (PAGE) to ensure purity. If purity was not desired, FUS fractions were pooled, diluted to reduce salt concentration, and re-ran the above protocol from CM Sepharose FF to HiTrap SP HP. Finally, FUS fractions with desired purity (Fig. S1) were pooled, aliquoted to 0.5 mL, flash frozen in liquid nitrogen, and stored in -80 °C freezer until refolding. For the first step in two-step refolding, 0.5 mL denatured FUS was thawed and diluted with 2 mL refolding buffer, 900 mM arginine, 100 mM [N-cyclohexyl-2-hydroxyl-3-aminopropanesulfonic acid] (CAPSO) pH 9.5, 0.3 mM reduced glutathione, 0.03 mM oxidized glutathione, and 1mM $ZnCl_2$, and stored over night at room temperature. The second step of refolding was performed during two rounds of two-hours dialysis against buffer D,10 % glycerol, 20 mM HEPES-NaOH pH 6.8, 300 mM NaCl, 0.1 mM EDTA, and 10mM BCD, with a SnakeSkin 10K MWCO dialysis tubing (Fisher) at room temperature. After concentrated with an Amicon 10K MWCO Ultra-4 centrifugal filter unit (Millipore Sigma), the protein concentration of the final product was measured on NanoDrop (Thermo Fisher) with an extinction coefficient of 70,140 $M^{-1}cm^{-1}$. The full-length tag-free FUS was aliquoted, flash frozen, and stored at -80°C.

To generate AlexaFluo488-labeled full-length tag-free FUS, a third round of dialysis was performed using a buffer D, pH adjusted to 7.5, right after the first two round of dialysis. AFDye 488 NHS Ester (Click Chemistry Tools) was added to FUS at a dye:protein molar ratio of 20:1 and incubated in dark at room temperature for 30 minutes. Ten rounds of buffer exchange to buffer D were performed using the above filter unit to ensure a complete removal of free dyes. Absorbance spectrum measured on NanoDrop was used to determine the labeling ratio and calculate the effective concentration of AlexaFluo488-labeled full-length tag-free FUS.

AlexaFlour647-labeled firefly luciferase (FL) mRNA was synthesized according to an established protocol[53,76]. A T7 promoter sequence (5'-TAATACGACTCACTATAGGG-3') was incorporated at the 5' end of the FL open reading frame during PCR amplification from a pRL-

CMV vector (Promega). A Kozak consensus sequence and a 50-nucleotide upstream region was incorporated before the translation start site to ensure enough space for the assembly of translation initiation complex[77]. After *in vitro* transcription with home-made T7 RNA polymerase, the transcript was purified via denaturing PAGE containing 7 M urea. The isolated RNA underwent enzymatic capping (NEB) and polyadenylation (Thermo Fisher), employing an initial incorporation of 2'-azido-2'-dATP (Jena Biosciences) followed by rATP. Finally, a click-chemistry reaction with AF647 sDIBO alkyne (Thermo Fisher) was conducted, strategically labeling between the coding sequence and the non-modified poly(A) tail to produce functional, fluorophore-conjugated FL mRNA. Free dyes were removed by multiple rounds of washing of the ethanol-precipitated mRNA pellet, which was confirmed by denaturing PAGE (Fig. S1).

FUS condensate assembly

A 10x phase separation buffer containing 200 mM tris(hydroxymethyl)aminomethane (Tris)-HCl, pH 7.5, 1000 mM NaCl, 20 mM DTT, and 10 mM $MgCl_2$ was prepared and filtered with a 0.22 μm syringe filter (Millipore Sigma) for all reconstitution experiments, which was adapted from prior phase separation studies of FUS. Condensates were reconstituted by thoroughly mixing the full-length tag-free FUS at a final concentration of 10 μM, a physiological concentration of FUS in Hela cell nucleus[39], with the phase separation buffer, an optional OSS, and any fluorescently labeled species based on experimental type #1-3 (Fig. 1h), as described below. Note that we keep the time between the assembly of condensates and imaging within 30 minutes, except for aging experiments (Fig. 4s-t), to ensure that all experimental observations reported in this study are signatures of early-stage condensates representing the dynamically assembled RNP granules in cells. Most importantly, we added the stock solution of FUS as the last component so that phase separation was initiated only after all other components were thoroughly mixed, mimicking the assembly of condensates within intracellular milieu. A total volume of 30 μL was used for each experiment.

For intra-condensate SMT or SPT with condensate boundary detection needed (Fig. 1h, #1), 10 nM AlexaFluo488-labeled FUS and 50 pM of the fluorescent species for SMT or SPT, such as Cy5 free dye, Cy5-labeled miRNA-21 (Integrated DNA Technologies), AlexaFlour647-labeled FL mRNA, 20-nm FluoSpheres Carboxylate-Modified Microspheres (Thermo Fisher), 9.5-nm CdSe/ZnS core-shell type QDs functionalized with carboxylic acid, PEG, or amine (Millipore Sigma), were mixed with phase separation buffer and an OSS composed of 2.4 mM protocatechuic acid (PCA), 24 nM protocatechuate-3,4-dioxygenase (PCD), and 2.4 mM Trolox[78] before adding stock solution of FUS. Cy5 free dye was made by neutralizing the N-hydroxysuccinimide (NHS) group on Cy5 NHS-ester (APExBIO) in 10 mM Tris-NaCl, pH 8.5 in dark at room temperature overnight. For the tracking of Cy5 free dye, single-Cy5-labeled miRNA-21, and the QDs, the PCA-PCD-Trolox OSS was omitted because these particles have low signal to noise ratio (SNR) due to fast-diffusion induced blurring, single-dye rather than multiple-dye labeling per molecule, and luminescence rather than fluorescence. For intra-condensate SMT of FUS, where condensate boundary detection was not needed because FUS single molecules in dilute phase cannot be tracked due to motion blurring by its fast diffusion (Fig. 1h, #2), 50 pM of AlexaFluo488-labeled FUS were mixed with phase separation buffer without OSS before adding stock solution of non-labeled full-length tag-free FUS. OSS was again omitted because AlexaFluo488-labeled FUS molecules have low SNR due to fast-diffusion, which we found could be further hindered by autofluorescence of high concentrations of PCA and Trolox in the OSS. However, for all SMT-PAINT experiments, extended SMT measurements were needed for an adequate coverage of trajectories over the intra-condensate space (Fig. 3f) and thus we implemented a color-less coupled glucose oxidase and catalase (GODCAT) OSS[78] with 55 U/mL glucose oxidase, 40 mM glucose, and 290 U/mL catalase. This

approach enabled us to obtain 10,000-frames long high-SNR SMT videos with much less autofluorescence than PCA and Trolox that fulfills SMT-PAINT reconstruction needs (Fig. S7). For intra-condensate SMT of FUS and RNA for dual-color SMT-PAINT reconstructions (Fig. 1h, #3), 50 pM of AlexaFluo488-labeled FUS and Cy5-labeled miRNA-21 or AlexaFluo647-labeled FL mRNA were mixed with phase separation buffer and GODCAT OSS before adding stock solution of non-labeled full-length tag-free FUS. For any experiments involved crowding or total RNA, Dextran T-500 (Millipore Sigma) was used at a final concentration of 10% (w/v) and Human HeLa Cell total RNA (TakaraBio) was used at a final concentration of 50 ng/μL.

Besides super-resolution imaging experiments above, FUS condensates were also assembled for phase diagram (Fig. S2), rheology measurements with C-Trap (Fig. 1c), z-stack imaging with an Alba5 time-resolved laser-scanning confocal microscope (ISS, Inc) (Fig. 1k), and fibrilization imaging (Fig. 4s) with minor modifications as listed below. For phase diagram, a 10x phase separation buffer was made without NaCl and $MgCl_2$ so both salt concentrations and FUS concentrations could be dictated by the combinations of conditions on phase diagram. C-Trap (LUMICKS) is an optical tweezer combined with laser scanning confocal microscope and thus could use fluorescence imaging to precisely measure condensate size change during fusion (Fig. 1c). For C-Trap experiments, a raised 200 nM concentration of AlexaFluo488-labeled FUS with the PCA-PCD-Trolox OSS described above were used to ensure adequate SNR of condensates during fast-scanning confocal imaging. For the z-stack imaging of condensates for the confirmation of 3D shape (Fig. 1k), an excess amount of red dye, 40 nM Cy5 free dye that can partition to FUS condensates, rather than AlexaFluo488-labeled FUS was used to simultaneously show the 3D shape of condensate and the location of glass slide, utilizing the intrinsic red autofluorescence of glass. Finally, for fibrilization imaging (Fig. 4s), FUS condensates were assembled without any OSS, crowding reagent, or fluorescent species to exclude the possibility that fibrilization is an artificial effect induced by any of them.

Microrheology

Condensate fusion events were measured on a u-Flux microfluidics chamber (LUMICKS) and thorough cleaning was needed before experiments. The u-Flux chamber was thoroughly flushed by Milli-Q water (Millipore Sigma), 6% hypo-chloride bleach solution, Milli-Q water again, and 0.5 M sodium thiosulfate to neutralize any remaining bleach. To prevent any unwanted protein-surface interactions, the u-Flux chamber was then sequentially flushed with 0.1% (w/v) bovine serum albumin (BSA) and 0.5% (w/v) Pluronic acid F-127 (Millipore Sigma). All flushes above were performed at 2 bars of pressure for at least 10 min under the control of the u-Flux microfluidics pumping system (LUMICKS) to ensure a thorough wash. The last flush before experiment was 1x phase separation buffer to match the solvent conditions of FUS condensates. Air bubbles in the chamber could perturb the lamina flow and thus it is critical to make sure the microfluidic chamber is free of bubbles before starting the experiment. If any bubble exists, 70% (v/v) ethanol solution was used to wash off air bubbles by changing surface tension, and all previous washing steps should be performed again to prepare chamber for the following measurement.

At least two channels within the u-Flux chamber were used for microrheology experiments, a condensate channel and a measurement channel. Condensates were assembled as described above and pumped into the condensate channel at a low pressure (<0.5 bar) to prevent the fission or deformation of condensates by friction forces, which can affect rheology measurements. Condensate fusion events were measured in the second measurement channel flowing with saturated concentration of 400 nM FUS determined from the phase diagram (Fig. S2) to avoid trapping additional free-floating condensates when moving the

probing trap. Condensates picked for microrheology measurement were all around 1 μm in diameter. The probing trap (purple, Fig. 1c) approached the measurement trap at a constant speed of 50 nm/s, which is slower than the condensate fusion time scale to provide adequate time for fusion. Force on the measurement trap (orange, Fig. 1c) was measured at 50 kHz while the confocal imaging was collected at 4 Hz, limited by the laser scanning speed and the size of a field of view (FOV) to cover the pair of condensates.

Analysis of force traces and confocal imaging were performed with home-made python scripts and Pylake package (LUMICKS). All home-made python scripts used in this section and below were all deposited at https://github.com/walterlab-um/intra_condensate_SPT. For confocal imaging data, condensate area was calculated by Otsu thresholding on fluorescence intensity, which has been proved to be the most accurate condensate boundary estimator among other computer vision methods for large condensates[58]. For force data, fusion events were identified by down sampling from 50 kHz to 5 Hz, calculating the gradient of force, and finding the largest peak in the gradient of force. For each fusion event, the original 50 kHz force data (F) was fitted to a previously used model[39,54]:

$$F = A + Be^{-\frac{t}{\tau}} + Ct$$

,where τ is the characteristic fusion time and A, B, C are constants. The exponential part is a theoretical formula for droplet fusion. Constant A describes background of force measurement while constant C describe the artificial force increase introduced by the interference between optical traps when probing trap approaches measurement trap at a constant speed. All fusion events were manually inspected before subjected to the above pipeline to exclude traces generated by non-fusing condensates or debris.

SMT/SPT under HILO microscope

Condensates assembled with fluorescent species as described above were tethered on a glass slide surface via a PEG-biotin:streptavidin:FUS-biotin tethering system we developed, where the surface passivation step has been published before[79]. Glass coverslips were thoroughly cleaned chemically via alkaline Piranha solution and physically with sonication. To achieve surface passivation via PEG functionalization, glass coverslips were then treated with 3-aminopropyltriethoxysilane (APTES, Millipore Sigma) with a 100:1 molar ratio mixture of 30 mM mPEG-succinimidyl valerate (SVA, Fisher) and 0.3 mM biotin-PEG-SVA, ended with a disuccinimidyl tartrate (DST, Thermo Fisher) treatment to neutralize any excess amount of reactive amine sites provided by APTES. Prepared slides were stored in a nitrogen tower in dark for up to 4 weeks. Right before experiments, sample wells (Fig. S14) were made from half-cut PCR tubes (Sigma-Aldrich) glued to the prepared slides with epoxy (Ellsworth Adhesives), and the PEG-biotin:streptavidin:FUS-biotin tethering system was established by incubating 1 mg/mL streptavidin (Thermo Fisher) and then 1 μM biotinylated FUS in sample wells for 15 minutes each, with three rounds of washing with T50 buffer, 10 mM Tris-HCl, 1 mm EDTA, pH 8.0, between each step to prevent interference by contamination (Fig. 1h). Note that the mPEG-SVA:biotin-PEG-SVA ratio was optimized to 100:1 to provide adequate tethers to restrict condensate motion while not inducing wetting. Once FUS condensates were added to each sample well, 50 μL of mineral oil was added dropwise on top of the mixture to prevent evaporation during imaging. The whole sample well was spun down at 200 g for 3 min to deposit FUS condensates to the glass surface for imaging later.

All SMT or SPT inside or outside of condensates were performed on an Nanoimager (Oxford) equipped with a 100x objective lens, a set of two emission filters (first with dual bands,

498-524 nm and 550-620 nm, and second with single band 665-705 nm), a 640 long-pass dichroic mirror channel splitter (the resulted two channels are referred to as green and red channel below), and a sCMOS camera. All videos have a pixel size of 117 nm. To reduce fluorescence background and increase SNR of single particles, highly inclined and laminated optical light-sheet (HILO)[55] microscopy was achieved by setting the excitation laser angle to 52°, where the total internal reflection (TIR) angle on our Nanoimager is around 53°. All imaging was performed at 24°C.

For intra-condensate SMT or SPT with condensate boundary detection needed (Fig. 1h, #1), SMT/SPT was performed in the red channel with 20 ms exposure time at an acquisition frequency of 50 Hz for the first 200 frames, excited by ~30 mW of 640 nm laser, while condensate bulk fluorescence imaging was performed in the green channel at the same exposure and frequency for the last 10 frames, excited by ~2 mW of 473 nm laser. The exposure time was optimized to 20 ms since a longer exposure time will hinder the tracking of fast-diffusing species by increasing motion blurring effect while a shorter exposure time will diminish SNR of single particles. Since condensates were tethered, their boundaries could be determined from an average intensity projection of the last 10 frames. For intra-condensate SMT of FUS without condensate boundary detection needs (Fig. 1h, #2), SMT of AlexaFluo488-labeled FUS was performed in the green channel at the same 20 ms exposure time and 50 Hz frequency for 200 frames, excited by ~30 mW of 473 nm laser. For intra-condensate SMT of FUS and RNA for dual-color SMT-PAINT reconstructions (Fig. 1h, #3), alternating-laser excitation (ALEX) of ~30 mW of 473 nm and 647 nm lasers were performed with 20 ms exposure time for each color, which translates to an effective acquisition frequency of 25 Hz for each color.

Finally, for SMT of FL mRNA outside condensates, both sample preparation and imaging procedures were slightly adjusted. Since FUS condensates strongly recruit RNAs, most mRNA molecules were inside condensates because of the relatively large condensed-phase volume at total FUS concentration of 10 μM. To allow more mRNA molecules observed outside condensates, we reduced the condensed phase volume by decreasing FUS concentration to 1 μM and lifted our focal plane to well above condensates, ensuring all molecules captured were outside condensates.

Phase diagram and fibrilization imaging

Phase diagram samples were prepared at various FUS concentrations of 0.5, 1.0, 2.0, and 5.0 μM. At each concentration we systematically varied the sodium chloride or potassium chloride salt concentrations of 0.1, 0.5, 0.75, and 1.0 M. For an accurate measurement for condensation near phase boundary of the phase diagram, an incubation time of one hour was used to give the protein-condensates adequate time to coarsen into a detectable size. Samples were imaged on an Olympus IX81 microscope equipped with a 100x oil-immersion objective with ~1 mW of 488 nm laser and an exposure time of 100 ms. Fibrilization imaging was performed in bright field at various time points of 0, 8, and 24 hours using the Nanoimager (Oxford) described above with a 100 ms exposure time.

Diffusion profiling pipeline

To pick up only single particle fluorescence signal while suppressing background, band-pass filtering on all SMT/SPT videos was achieved by applying a difference of Gaussian (DoG) filter with a lower sigma of 1 pixel and a higher sigma of 3 pixels, representing on-focus and slightly off-focus single molecules. Filtered videos were subjected to TrackMate[80] to detect spots and extract trajectories. Spot detection was performed with a Laplacian of Gaussian (LoG) detector,

where an estimated object diameter was set to 5 pixels (585 nm) and a spot quality threshold set to 5 or determined by the peak of false-positive spots in the distribution of quality values (Fig. S15). Trajectories were extracted by classic particle-linking algorithm, Linear Assignment Problem (LAP), with the following parameter settings: for intra-condensate tracking, linking maximum distance was set to 5 pixels (585 nm) with no gaps allowed; for dilute-phase tracking, linking maximum distance was set to 15 pixels (1.755 μm) with no gaps allowed. Trajectories were exported as csv files and fed to home-made python scripts for diffusion profiling.

Our diffusion profiling pipeline has two parts: discrete categorization and continuous spectrum (Fig. 2a-f). The discrete categorization part classifies every trajectory as either immobile, confined, or normal diffusion by following steps. To determine whether the particle is immobile or not, mean step size of each trajectory was calculated and compared to a threshold of 30 nm based on the 16 nm static localization error calculated from static mRNA molecules attached to glass surface (Fig. S4). To determine whether a mobile particle is confined or not, anomalous diffusion component α was calculated by fitting the mean squared displacement (MSD)-lag time (τ) curve on a log-log scale using the formula below.

$$log(MSD) = \alpha\, log(\tau) + log(2nD)$$

where n is the dimension of tracking ($n = 2$ in our case) and D is the diffusion coefficient. Note that the optimal number of fitting points in an MSD-τ fitting has been determined to be roughly half of the trajectory length[81], and thus we performed the fitting with a MSD-τ series with the biggest τ is smaller than half trajectory length unless it's shorter than 5 steps, where a minimal number of 4 MSD-τ points were guaranteed for accurate fitting. Trajectories that did not fit well to the model, indicated by fitting $R^2 < 0.7$, were removed from the pool when calculating diffusion type fractions. Trajectories with $\alpha < 0.7$ were categorized as confined diffusion while $\alpha > 0.7$ as normal diffusion. Notably, we found that trajectories with very small α were also having very small R2 and thus the removal of the bad-fitting trajectories also removed trajectories with extremely small α (Fig. S16).

The continuous spectrum part generates distributions of mean step size, α, angle between steps, apparent diffusion coefficient D_{app}, and localization error. The mean step size was calculated for all trajectories. The α components were calculated as described above for only mobile trajectories. The angle between steps was defined as the angle between the previous and current step ranging from 0°, meaning no change in direction, to 180°, meaning a complete turn-back, regardless of left or right and was also calculated for all mobile trajectories. The D_{app} and localization error were calculated for non-confined trajectories by fitting MSD-τ curve to the following formula, which is optimized for least-square fit of MSD[81,82]:

$$MSD = 2nD\tau + 2\sigma^2 - 4DR\tau$$

where σ is the localization error and R is the motion blur coefficient ($R = 1/6$ for continuous imaging as in our case). A Bayesian statistics-based state array method (saSPT[60]) was used to obtain a D_{app} spectrum with higher resolution, which originates from the fact that saSPT interprets D_{app} and localization error from each single step rather than a whole trajectory as above. Most parameters in saSPT were set to default values except that the range of diffusion coefficient in state array specified in "constants.py" file was changed accordingly.

SMT-PAINT and step size heatmap analysis

Point accumulation reconstruction was performed with home-made python scripts on 10,000-frames long SMT videos collected from SMT-PAINT experiments (Fig. 1h, #2-3) as described above. To ensure that puncta in SMT-PAINT images reveal underlying intra-condensate architecture that confines diffusion, the oversampling from long trajectories needs to be suppressed, avoiding the formation of artificial puncta due to a single long trajectory. Therefore, when generating the pool of locations for the reconstruction, only 10 locations were randomly sampled from all locations for any trajectory longer than 10 steps while all locations from trajectories shorter than 10 steps were passed along. SMT-PAINT image of the whole FOV was rendered by binning the pool of locations back to a grid of 117-nm pixels, the same as the input SMT-PAINT video. Similarly, step size heatmap image of the whole FOV was generated from the pool above, by calculating pixel-by-pixel the mean for all steps that have a center of step within the pixel. Drift correction was not needed given the short total length of imaging time (200 s).

Not all condensates were subjected to downstream analysis because some condensates did not have enough trajectories to cover the whole condensate while others had a strip-like pattern due to 'lensing effect', where the spherical shape of condensates works as a lens to skew illumination (Fig. S17). Therefore, qualified condensates were picked by a python script followed by manual inspection. The python script first generates contours for all condensates by applying a threshold of 10 locations per pixel to the whole-FOV SMT-PAINT image smoothed with a $\sigma = 1$ Gaussian kernel. The whole-FOV SMT-PAINT image was split to individual-condensate SMT-PAINT images by filtering out condensates smaller than 200 pixel^2 and cropping out each remaining condensate with a surrounding box with a padding distance of 3 pixels. All individual-condensate SMT-PAINT images were manually inspected to leave out all condensates with unwanted strip-like pattern (Fig. S17)

SMT-PAINT and step size heatmap images of all qualified condensates were paired, such as SMT-PAINT images of FUS versus mRNA, step size heatmap of FUS versus mRNA, and SMT-PAINT versus step size heatmap images of FUS, and analyzed with weighted pixel-wise Pearson correlation coefficient (PCC) using the below formula:

$$PCC_{weighted} = \frac{\sum_i w_i (x_i - \bar{x})(y_i - \bar{y})}{\sqrt{(\sum_i w_i (x_i - \bar{x})^2)(\sum_i w_i (y_i - \bar{y})^2)}}$$

where x_i and y_i are the value of i-th pixel in the vectorized (X, Y) image pair, $\bar{x}$ and $\bar{y}$ are the mean of all pixels in the X or Y image, and w_i is the weight of i-th pixel in the same vectorized image. X and Y image in the (X, Y) image pair can be either SMT-PAINT image, where pixel value is number of locations, or step size heatmap image, where pixel value is mean step size. Weight is set to be the square of number of locations per pixel, factoring in that pixel values coming from more trajectories are more reliable than those coming from less trajectories.

Pair-correlation functions

Spatial distribution of SMT trajectories within a condensate was analyzed by the auto- or cross-pair correlation function $G_{auto}(r)$ or $G_{cross}(r)$ (a.k.a. radial distribution function) of locations. Pair correlation function $G(r)$ describes the probability of finding a particle of interest at a distance r from a reference particle, where the reference particle and the particle of interest are of same type in $G_{auto}(r)$ but are of different type in $G_{cross}(r)$. Pair correlation function can be calculated by

$$G(r) = \frac{N_{interest}(r)}{N_{ref} \cdot \rho_{interest} \cdot 2\pi r \cdot dr}$$

where function $N_{interest}(r)$ counts the number of particles of interest that are r to $r + dr$ away from reference particles in a condensate, N_{ref} is the total number of reference particles in a condensate, $\rho_{interest}$ is the density of particles of interest in a condensate, and $2\pi r \cdot dr$ is the ring area that normalizes the excess number of particles counted by function $N_{interest}(r)$ as the ring area scales with r.

In the python script, $N_{interest}(r)$ was calculated by iterating through all reference particles because the normalization factor needs to be adjusted when the reference particle was too close to the condensate boundary. In that case, the ring centered at the reference particle was partially outside the condensate, where no particles of interest can be found, and thus it would be wrong to assume an average number of counts of $\rho_{interest} \cdot 2\pi r \cdot dr$ can be found in the ring. Therefore, for all reference particles closer to the condensate boundary than $r + dr$, the ring area within condensate was calculated to substitute $2\pi r \cdot dr$ in the above equation. For all $G(r)$ in this study, dr was kept at 100 nm and r ranged from 0 to 1 μm, with a sliding-window of 20 nm between adjacent r.

Every qualified condensate yielded a $G(r)$ and the $G(r)$ for all plots was a weighted average of all the individual-condensate $G(r)$, with the weight being total number of particles within each condensate. Each individual-condensate $G(r)$ was then fitted to the exponential model below because exponential decay can depict the behavior of molecules in a phase-transition system[83]:

$$G(r) = 1 + Ae^{-\frac{r}{R}}$$

where A is the amplitude that describes how much more or less likely a particle could be found compared to a random distribution of particles, and R is the characteristic radius of the clustering of particles. A parametric bootstrapping, 5,000 rounds of re-sampling from the pool of individual-condensate $G(r)$, was performed to estimate the A and R for each experiment and their confidence intervals. A and R in each bootstrapping round were also plotted as histograms.

Spatial distributions of nanodomains

Nanodomains locations were estimated by either puncta detected by a LoG spot detector on individual-condensate SMT-PAINT images or using the centroid of confined FUS or RNA trajectories within a condensate. The distance of all such locations within a condensate to the center of the condensate was normalized by the radius of the condensate, where the radius was calculated from the total area of the condensate assuming a circular shape. Similar to $G(r)$, the distribution of all such distances within a condensate was also biased by the ring area growing with r, and thus needed to be normalized by ring area using:

$$P_{norm}(r) = \frac{P(r)}{\rho_{interest} \cdot 2\pi r \cdot dr}$$

where $P(r)$ and $P_{norm}(r)$ are the probability and the normalized probability of distances that are r to $r + dr$ away from the condensate center, $\rho_{interest}$ is the density of particles of interest in the condensate, and $2\pi r \cdot dr$ is the ring area. Every qualified condensate yielded a $P_{norm}(r)$, and 5,000 rounds of non-parametric bootstrapping from the pool of individual-condensate $P_{norm}(r)$ were performed to estimate the mean of $P_{norm}(r)$ for every r.

Fluorescence lifetime imaging and correlation spectroscopy

Fluorescence lifetime imaging (FLIM) imaging of tethered condensates was performed with an Alba5 time-resolved laser-scanning confocal microscope (ISS, Inc) with a pulsed supercontinuum broadband laser excitation source (Fianium WhiteLase SC-400-8-PP), avalanche photodiode (APD) detectors, and a Beckr-Hickl SPC-830 TCSPC module. Condensates tethered on the glass surface were first found under regular scanning confocal imaging mode. After an optimal field of view framing a single condensate was identified, ten rounds of FLIM scanning throughout the whole filed of view were performed to ensure adequate data points for the lifetime calculation via deconvolution and fitting to a reference instrument response function (IRF) using FLIMfit[84]. The number of FLIM scans on each condensate was carefully chosen to achieve a total imaging time of around five minutes, matching a time scale where nanodomains were relatively immobile as revealed by time-lapse SMT-PAINT.

The coupled fluorescence correlation spectroscopy (FCS) with FLIM assay was performed with the same setup as above, but only ten locations within each condensate were chosen at random using Sobel sampling rather than scanning through the whole condensate as in FLIM imaging. One-minute-long time-resolved intensity traces for Alexa488-labeled full-length tag-free FUS were acquired per location and analyzed both for diffusion coefficient using FCS as well as fluorescent lifetime. Lifetime fitting was done with a MATLAB package FluoFit[85], while FCS curves were analyzed with a custom MATLAB implementation of a segmented autocorrelation algorithm[86] to reduce the effect of photobleaching or long-term diffusive effects such as rocking of the condensate droplet as a whole. Note that the one-minute-long FCS traces provide much more datapoints for FLIM fitting compared to each pixel in a FLIM image, resulting in a better fit and explaining the different ranges of lifetime in FLIM imaging versus FCS-FLIM assays.

Acknowledgement

We thank Sujay Ray, Ziyuan Chen, Adam Decker, Nat Rogers, and Xiaofeng Dai for their insightful discussions on developing the analysis pipelines for our SMT datasets. We appreciate help from Damon Hoff of the Single Molecule Analysis in Real-Time (SMART) Center of Biophysics at the University of Michigan for FLIM and FCS measurements and analysis, and Ehsan Akbari and Denis Pelekhov at the Nano-Systems Laboratory (NSL) of the Physics department at the Ohio State University for their help in using a Lumicks C-Trap for condensate microrheology measurements. We much appreciate the invaluable feedback and proofreading efforts from Ziyuan Chen, Adrien Chauvier, Yi Zhu, Sicong Ma, and Minjun Jin. We also thank Liuhan Dai for his early joint efforts in protein purification and Mohammed Hijaz for help with quantifying the translatability of FL mRNAs. Lastly, we acknowledge the University of Michigan UM-GPT for proofreading and grammar edits using a GPT-4.0 Turbo model.

References

1 Mittag, T. & Pappu, R. V. A conceptual framework for understanding phase separation and addressing open questions and challenges. *Mol Cell* **82**, 2201-2214 (2022). https://doi.org/10.1016/j.molcel.2022.05.018

2 Roden, C. & Gladfelter, A. S. RNA contributions to the form and function of biomolecular condensates. *Nat Rev Mol Cell Biol* **22**, 183-195 (2021). https://doi.org/10.1038/s41580-020-0264-6

3 Pitchiaya, S. *et al.* Dynamic Recruitment of Single RNAs to Processing Bodies Depends on RNA Functionality. *Mol Cell* **74**, 521-533 e526 (2019). https://doi.org/10.1016/j.molcel.2019.03.001

4 Bressloff, P. C. & Newby, J. M. Stochastic models of intracellular transport. *Rev Mod Phys* **85**, 135-196 (2013). https://doi.org/10.1103/RevModPhys.85.135

5 Portz, B., Lee, B. L. & Shorter, J. FUS and TDP-43 Phases in Health and Disease. *Trends Biochem Sci* **46**, 550-563 (2021). https://doi.org/10.1016/j.tibs.2020.12.005

6 Giannone, G. *et al.* Dynamic superresolution imaging of endogenous proteins on living cells at ultra-high density. *Biophys J* **99**, 1303-1310 (2010). https://doi.org/10.1016/j.bpj.2010.06.005

7 Pappu, R. V., Cohen, S. R., Dar, F., Farag, M. & Kar, M. Phase Transitions of Associative Biomacromolecules. *Chem Rev* **123**, 8945-8987 (2023). https://doi.org/10.1021/acs.chemrev.2c00814

8 Lyon, A. S., Peeples, W. B. & Rosen, M. K. A framework for understanding the functions of biomolecular condensates across scales. *Nat Rev Mol Cell Biol* **22**, 215-235 (2021). https://doi.org/10.1038/s41580-020-00303-z

9 Alberti, S. & Hyman, A. A. Biomolecular condensates at the nexus of cellular stress, protein aggregation disease and ageing. *Nat Rev Mol Cell Biol* **22**, 196-213 (2021). https://doi.org/10.1038/s41580-020-00326-6

10 Hwang, D. W., Maekiniemi, A., Singer, R. H. & Sato, H. Real-time single-molecule imaging of transcriptional regulatory networks in living cells. *Nat Rev Genet* (2024). https://doi.org/10.1038/s41576-023-00684-9

11 Sharp, P. A., Chakraborty, A. K., Henninger, J. E. & Young, R. A. RNA in formation and regulation of transcriptional condensates. *RNA* **28**, 52-57 (2022). https://doi.org/10.1261/rna.078997.121

12 Guo, Y. E. *et al.* Pol II phosphorylation regulates a switch between transcriptional and splicing condensates. *Nature* **572**, 543-548 (2019). https://doi.org/10.1038/s41586-019-1464-0

13 Li, W. *et al.* Biophysical properties of AKAP95 protein condensates regulate splicing and tumorigenesis. *Nat Cell Biol* **22**, 960-972 (2020). https://doi.org/10.1038/s41556-020-0550-8

14 Xu, S. *et al.* SRRM2 organizes splicing condensates to regulate alternative splicing. *Nucleic Acids Res* **50**, 8599-8614 (2022). https://doi.org/10.1093/nar/gkac669

15 Zhuang, Y. *et al.* Circadian clocks are modulated by compartmentalized oscillating translation. *Cell* **186**, 3245-3260 e3223 (2023). https://doi.org/10.1016/j.cell.2023.05.045

16 Nosella, M. L. & Forman-Kay, J. D. Phosphorylation-dependent regulation of messenger RNA transcription, processing and translation within biomolecular condensates. *Curr Opin Cell Biol* **69**, 30-40 (2021). https://doi.org/10.1016/j.ceb.2020.12.007

17 Tibble, R. W., Depaix, A., Kowalska, J., Jemielity, J. & Gross, J. D. Biomolecular condensates amplify mRNA decapping by biasing enzyme conformation. *Nat Chem Biol* **17**, 615-623 (2021). https://doi.org/10.1038/s41589-021-00774-x

18 Cougot, N., Babajko, S. & Seraphin, B. Cytoplasmic foci are sites of mRNA decay in human cells. *J Cell Biol* **165**, 31-40 (2004). https://doi.org/10.1083/jcb.200309008

19 Ditlev, J. A., Case, L. B. & Rosen, M. K. Who's In and Who's Out-Compositional Control of Biomolecular Condensates. *J Mol Biol* **430**, 4666-4684 (2018). https://doi.org/10.1016/j.jmb.2018.08.003

20 Banani, S. F., Lee, H. O., Hyman, A. A. & Rosen, M. K. Biomolecular condensates: organizers of cellular biochemistry. *Nat Rev Mol Cell Biol* **18**, 285-298 (2017). https://doi.org/10.1038/nrm.2017.7

21 Peeples, W. & Rosen, M. K. Mechanistic dissection of increased enzymatic rate in a phase-separated compartment. *Nat Chem Biol* **17**, 693-702 (2021). https://doi.org/10.1038/s41589-021-00801-x

22 Collins, M. J., Tomares, D. T., Nandana, V., Schrader, J. M. & Childers, W. S. RNase E biomolecular condensates stimulate PNPase activity. *Sci Rep* **13**, 12937 (2023). https://doi.org/10.1038/s41598-023-39565-w

23 Mateju, D. *et al.* Single-Molecule Imaging Reveals Translation of mRNAs Localized to Stress Granules. *Cell* **183**, 1801-1812 e1813 (2020). https://doi.org/10.1016/j.cell.2020.11.010

24 Wilbertz, J. H. *et al.* Single-Molecule Imaging of mRNA Localization and Regulation during the Integrated Stress Response. *Mol Cell* **73**, 946-958 e947 (2019). https://doi.org/10.1016/j.molcel.2018.12.006

25 Moon, S. L. *et al.* Multicolour single-molecule tracking of mRNA interactions with RNP granules. *Nat Cell Biol* **21**, 162-168 (2019). https://doi.org/10.1038/s41556-018-0263-4

26 Wu, T., King, M. R., Farag, M., Pappu, R. V. & Lew, M. D. Single fluorogen imaging reveals distinct environmental and structural features of biomolecular condensates. *bioRxiv* (2023). https://doi.org/10.1101/2023.01.26.525727

27 Kamagata, K., Kusano, R., Kanbayashi, S., Banerjee, T. & Takahashi, H. Single-molecule characterization of target search dynamics of DNA-binding proteins in DNA-condensed droplets. *Nucleic Acids Res* **51**, 6654-6667 (2023). https://doi.org/10.1093/nar/gkad471

28 He, C., Wu, C. Y., Li, W. & Xu, K. Multidimensional Super-Resolution Microscopy Unveils Nanoscale Surface Aggregates in the Aging of FUS Condensates. *J Am Chem Soc* **145**, 24240-24248 (2023). https://doi.org/10.1021/jacs.3c08674

29 Galvanetto, N. *et al.* Extreme dynamics in a biomolecular condensate. *Nature* **619**, 876-883 (2023). https://doi.org/10.1038/s41586-023-06329-5

30 Kamagata, K. *et al.* Structure-dependent recruitment and diffusion of guest proteins in liquid droplets of FUS. *Sci Rep* **12**, 7101 (2022). https://doi.org/10.1038/s41598-022-11177-w

31 Kamagata, K. *et al.* Molecular principles of recruitment and dynamics of guest proteins in liquid droplets. *Sci Rep* **11**, 19323 (2021). https://doi.org/10.1038/s41598-021-98955-0

32 Shen, Z. *et al.* Biological condensates form percolated networks with molecular motion properties distinctly different from dilute solutions. *Elife* **12** (2023). https://doi.org/10.7554/eLife.81907

33 Yao, R. W. & Rosen, M. K. Advanced Surface Passivation for High-Sensitivity Studies of Biomolecular Condensates. *bioRxiv* (2024). https://doi.org/10.1101/2024.02.12.580000

34 Snead, W. T. *et al.* Membrane surfaces regulate assembly of ribonucleoprotein condensates. *Nat Cell Biol* **24**, 461-470 (2022). https://doi.org/10.1038/s41556-022-00882-3

35 Yuan, F. *et al.* Membrane bending by protein phase separation. *Proc Natl Acad Sci U S A* **118** (2021). https://doi.org/10.1073/pnas.2017435118

36 Rouches, M., Veatch, S. L. & Machta, B. B. Surface densities prewet a near-critical membrane. *Proc Natl Acad Sci U S A* **118** (2021). https://doi.org/10.1073/pnas.2103401118

37 Zuo, L. *et al.* Loci-specific phase separation of FET fusion oncoproteins promotes gene transcription. *Nat Commun* **12**, 1491 (2021). https://doi.org/10.1038/s41467-021-21690-7

38 Levone, B. R. *et al.* FUS-dependent liquid-liquid phase separation is important for DNA repair initiation. *J Cell Biol* **220** (2021). https://doi.org/10.1083/jcb.202008030

39 Patel, A. *et al.* A Liquid-to-Solid Phase Transition of the ALS Protein FUS Accelerated by Disease Mutation. *Cell* **162**, 1066-1077 (2015). https://doi.org/10.1016/j.cell.2015.07.047

40 Wang, W. Y. *et al.* Interaction of FUS and HDAC1 regulates DNA damage response and repair in neurons. *Nat Neurosci* **16**, 1383-1391 (2013). https://doi.org/10.1038/nn.3514
41 Kwiatkowski, T. J., Jr. *et al.* Mutations in the FUS/TLS gene on chromosome 16 cause familial amyotrophic lateral sclerosis. *Science* **323**, 1205-1208 (2009). https://doi.org/10.1126/science.1166066
42 Vance, C. *et al.* Mutations in FUS, an RNA processing protein, cause familial amyotrophic lateral sclerosis type 6. *Science* **323**, 1208-1211 (2009). https://doi.org/10.1126/science.1165942
43 Mackenzie, I. R., Rademakers, R. & Neumann, M. TDP-43 and FUS in amyotrophic lateral sclerosis and frontotemporal dementia. *Lancet Neurol* **9**, 995-1007 (2010). https://doi.org/10.1016/S1474-4422(10)70195-2
44 Lagier-Tourenne, C. *et al.* Divergent roles of ALS-linked proteins FUS/TLS and TDP-43 intersect in processing long pre-mRNAs. *Nat Neurosci* **15**, 1488-1497 (2012). https://doi.org/10.1038/nn.3230
45 Deng, H., Gao, K. & Jankovic, J. The role of FUS gene variants in neurodegenerative diseases. *Nat Rev Neurol* **10**, 337-348 (2014). https://doi.org/10.1038/nrneurol.2014.78
46 Ishiguro, A., Katayama, A. & Ishihama, A. Different recognition modes of G-quadruplex RNA between two ALS/FTLD-linked proteins TDP-43 and FUS. *FEBS Lett* **595**, 310-323 (2021). https://doi.org/10.1002/1873-3468.14013
47 Ishiguro, A., Lu, J., Ozawa, D., Nagai, Y. & Ishihama, A. ALS-linked FUS mutations dysregulate G-quadruplex-dependent liquid-liquid phase separation and liquid-to-solid transition. *J Biol Chem* **297**, 101284 (2021). https://doi.org/10.1016/j.jbc.2021.101284
48 Alberti, S. *et al.* A User's Guide for Phase Separation Assays with Purified Proteins. *J Mol Biol* **430**, 4806-4820 (2018). https://doi.org/10.1016/j.jmb.2018.06.038
49 Monahan, Z. *et al.* Phosphorylation of the FUS low-complexity domain disrupts phase separation, aggregation, and toxicity. *EMBO J* **36**, 2951-2967 (2017). https://doi.org/10.15252/embj.201696394
50 Murthy, A. C. *et al.* Molecular interactions underlying liquid-liquid phase separation of the FUS low-complexity domain. *Nat Struct Mol Biol* **26**, 637-648 (2019). https://doi.org/10.1038/s41594-019-0250-x
51 Murray, D. T. *et al.* Structure of FUS Protein Fibrils and Its Relevance to Self-Assembly and Phase Separation of Low-Complexity Domains. *Cell* **171**, 615-627 e616 (2017). https://doi.org/10.1016/j.cell.2017.08.048
52 Wang, J. *et al.* A Molecular Grammar Governing the Driving Forces for Phase Separation of Prion-like RNA Binding Proteins. *Cell* **174**, 688-699 e616 (2018). https://doi.org/10.1016/j.cell.2018.06.006
53 Custer, T. C. & Walter, N. G. In vitro labeling strategies for in cellulo fluorescence microscopy of single ribonucleoprotein machines. *Protein Sci* **26**, 1363-1379 (2017). https://doi.org/10.1002/pro.3108
54 Kaur, T. *et al.* Molecular Crowding Tunes Material States of Ribonucleoprotein Condensates. *Biomolecules* **9** (2019). https://doi.org/10.3390/biom9020071
55 Tokunaga, M., Imamoto, N. & Sakata-Sogawa, K. Highly inclined thin illumination enables clear single-molecule imaging in cells. *Nat Methods* **5**, 159-161 (2008). https://doi.org/10.1038/nmeth1171
56 Sanders, D. W. *et al.* Competing Protein-RNA Interaction Networks Control Multiphase Intracellular Organization. *Cell* **181**, 306-324 e328 (2020). https://doi.org/10.1016/j.cell.2020.03.050
57 Eisenberg, D., Schwarz, E., Komaromy, M. & Wall, R. Analysis of membrane and surface protein sequences with the hydrophobic moment plot. *J Mol Biol* **179**, 125-142 (1984). https://doi.org/10.1016/0022-2836(84)90309-7

58 Gao, G. & Walter, N. G. Critical Assessment of Condensate Boundaries in Dual-Color Single Particle Tracking. *J Phys Chem B* **127**, 7694-7707 (2023). https://doi.org/10.1021/acs.jpcb.3c03776

59 Burnecki, K., Kepten, E., Garini, Y., Sikora, G. & Weron, A. Estimating the anomalous diffusion exponent for single particle tracking data with measurement errors - An alternative approach. *Sci Rep* **5**, 11306 (2015). https://doi.org/10.1038/srep11306

60 Heckert, A., Dahal, L., Tjian, R. & Darzacq, X. Recovering mixtures of fast-diffusing states from short single-particle trajectories. *Elife* **11** (2022). https://doi.org/10.7554/eLife.70169

61 Gopal, A., Zhou, Z. H., Knobler, C. M. & Gelbart, W. M. Visualizing large RNA molecules in solution. *RNA* **18**, 284-299 (2012). https://doi.org/10.1261/rna.027557.111

62 Berezin, M. Y. & Achilefu, S. Fluorescence lifetime measurements and biological imaging. *Chem Rev* **110**, 2641-2684 (2010). https://doi.org/10.1021/cr900343z

63 Emmanouilidis, L. *et al.* A solid beta-sheet structure is formed at the surface of FUS droplets during aging. *Nat Chem Biol* (2024). https://doi.org/10.1038/s41589-024-01573-w

64 Shen, Y. *et al.* The liquid-to-solid transition of FUS is promoted by the condensate surface. *Proc Natl Acad Sci U S A* **120**, e2301366120 (2023). https://doi.org/10.1073/pnas.2301366120

65 Khong, A. *et al.* The Stress Granule Transcriptome Reveals Principles of mRNA Accumulation in Stress Granules. *Mol Cell* **68**, 808-820 e805 (2017). https://doi.org/10.1016/j.molcel.2017.10.015

66 Hubstenberger, A. *et al.* P-Body Purification Reveals the Condensation of Repressed mRNA Regulons. *Mol Cell* **68**, 144-157 e145 (2017). https://doi.org/10.1016/j.molcel.2017.09.003

67 Glauninger, H., Wong Hickernell, C. J., Bard, J. A. M. & Drummond, D. A. Stressful steps: Progress and challenges in understanding stress-induced mRNA condensation and accumulation in stress granules. *Mol Cell* **82**, 2544-2556 (2022). https://doi.org/10.1016/j.molcel.2022.05.014

68 Zanetti-Domingues, L. C., Tynan, C. J., Rolfe, D. J., Clarke, D. T. & Martin-Fernandez, M. Hydrophobic fluorescent probes introduce artifacts into single molecule tracking experiments due to non-specific binding. *PLoS One* **8**, e74200 (2013). https://doi.org/10.1371/journal.pone.0074200

69 Todorov, T. I., de Carmejane, O., Walter, N. G. & Morris, M. D. Capillary electrophoresis of RNA in dilute and semidilute polymer solutions. *Electrophoresis* **22**, 2442-2447 (2001). https://doi.org/10.1002/1522-2683(200107)22:12<2442::AID-ELPS2442>3.0.CO;2-9

70 Lafontaine, D. L. J., Riback, J. A., Bascetin, R. & Brangwynne, C. P. The nucleolus as a multiphase liquid condensate. *Nat Rev Mol Cell Biol* **22**, 165-182 (2021). https://doi.org/10.1038/s41580-020-0272-6

71 Erkamp, N. A. *et al.* Spatially non-uniform condensates emerge from dynamically arrested phase separation. *Nat Commun* **14**, 684 (2023). https://doi.org/10.1038/s41467-023-36059-1

72 Seim, I. *et al.* Dilute phase oligomerization can oppose phase separation and modulate material properties of a ribonucleoprotein condensate. *Proc Natl Acad Sci U S A* **119**, e2120799119 (2022). https://doi.org/10.1073/pnas.2120799119

73 Wadsworth, G. M. *et al.* RNAs undergo phase transitions with lower critical solution temperatures. *Nat Chem* **15**, 1693-1704 (2023). https://doi.org/10.1038/s41557-023-01353-4

74 Lin, A. Z. *et al.* Dynamical control enables the formation of demixed biomolecular condensates. *Nat Commun* **14**, 7678 (2023). https://doi.org/10.1038/s41467-023-43489-4

75 Joshi, A. *et al.* Single-molecule FRET unmasks structural subpopulations and crucial molecular events during FUS low-complexity domain phase separation. *Nat Commun* **14**, 7331 (2023). https://doi.org/10.1038/s41467-023-43225-y

76 Schmidt, A., Gao, G., Little, S. R., Jalihal, A. P. & Walter, N. G. Following the messenger: Recent innovations in live cell single molecule fluorescence imaging. *Wiley Interdiscip Rev RNA* **11**, e1587 (2020). https://doi.org/10.1002/wrna.1587

77 Brito Querido, J. *et al.* Structure of a human 48S translational initiation complex. *Science* **369**, 1220-1227 (2020). https://doi.org/10.1126/science.aba4904

78 Aitken, C. E., Marshall, R. A. & Puglisi, J. D. An oxygen scavenging system for improvement of dye stability in single-molecule fluorescence experiments. *Biophys J* **94**, 1826-1835 (2008). https://doi.org/10.1529/biophysj.107.117689

79 Johnson-Buck, A. *et al.* Kinetic fingerprinting to identify and count single nucleic acids. *Nat Biotechnol* **33**, 730-732 (2015). https://doi.org/10.1038/nbt.3246

80 Tinevez, J. Y. *et al.* TrackMate: An open and extensible platform for single-particle tracking. *Methods* **115**, 80-90 (2017). https://doi.org/10.1016/j.ymeth.2016.09.016

81 Michalet, X. & Berglund, A. J. Optimal diffusion coefficient estimation in single-particle tracking. *Phys Rev E Stat Nonlin Soft Matter Phys* **85**, 061916 (2012). https://doi.org/10.1103/PhysRevE.85.061916

82 Berglund, A. J. Statistics of camera-based single-particle tracking. *Phys Rev E Stat Nonlin Soft Matter Phys* **82**, 011917 (2010). https://doi.org/10.1103/PhysRevE.82.011917

83 Veatch, S. L. *et al.* Correlation functions quantify super-resolution images and estimate apparent clustering due to over-counting. *PLoS One* **7**, e31457 (2012). https://doi.org/10.1371/journal.pone.0031457

84 Warren, S. C. *et al.* Rapid Global Fitting of Large Fluorescence Lifetime Imaging Microscopy Datasets. *Plos One* **8** (2013). https://doi.org/ARTN e70687

10.1371/journal.pone.0070687

85 Enderlein, J. & Erdmann, R. Fast fitting of multi-exponential decay curves. *Opt Commun* **134**, 371-378 (1997). https://doi.org/Doi 10.1016/S0030-4018(96)00384-7

86 Kohler, J., Hur, K. H. & Mueller, J. D. Autocorrelation function of finite-length data in fluorescence correlation spectroscopy. *Biophys J* **122**, 241-253 (2023). https://doi.org/10.1016/j.bpj.2022.10.027